Chapter 15
Topological Dynamics of Spin Texture Based Metamaterials

Zhixiong Li, Yunshan Cao, and Peng Yan

Abstract Pursuing topological phase and matter in a variety of systems is one central issue in current physical sciences and engineering. Similar to other (quasi-)particles, the collective gyration motion of magnetic spin textures (vortex, bubble, and skyrmion etc.) can also exhibit the behavior of waves. In this chapter, we review our recent work on topological dynamics of spin-texture based metamaterials. We first briefly introduce the topological structures, properties, and applications of magnetic solitons. Then we focus on the topological dynamics of spin texture lattice, uncovering the first-order topological insulator in two-dimensional honeycomb lattice of massive magnetic skyrmions, and the second-order topological insulator in breathing kagome and honeycomb lattice of vortices. Conclusion and outlook are drawn finally.

15.1 Introduction

In recent years, topological insulators (TIs) [1–3] are receiving considerable attention for their exotic physical properties. The most peculiar character of TIs is that they can support chiral edge states which are absent in conventional insulators. Topological edge states are modes confined at the boundary/surface of a system and generally have a certain chirality which enables them to be immune from small disturbances such as disorders and/or defects. Ever since its discovery in electronic systems [4, 5], the topological edge state has been readily predicted and observed in optics [6–10], mechanics [11–14], acoustics [15–18], and very recently in magnetics [19–22].

A conventional n-dimensional topological insulator only has $(n-1)$-dimensional (first-order) topological edge/surface modes according to the bulk-boundary correspondence [1, 2]. Very recently, the concept of higher-order topological insulators (HOTIs) was proposed [23–29] and confirmed by various experiments in

Z. Li · Y. Cao · P. Yan (✉)
School of Electronic Science and Engineering, University of Electronic Science and Technology of China, Chengdu 610054, China
e-mail: yan@uestc.edu.cn

E. Kamenetskii (ed.), *Chirality, Magnetism and Magnetoelectricity*,
Topics in Applied Physics 138,
https://doi.org/10.1007/978-3-030-62844-4_15

photonic [30–35], acoustic [36–40], and electric-circuit [41–45] systems. Different from first-order topological insulators (FOTIs), a HOTI has $(n-2)$ or even $(n-3)$-dimensional (second-order or third-order) topological boundary states, which goes beyond the conventional bulk-boundary correspondence and is characterized by several new topological invariants, such as the nested Wilson loop [46], Green's function zeros [47], the quantized bulk polarization (Wannier center) [25, 36, 37], and the $\mathbb{Z}_N$ Berry phase (quantized to $2\pi/N$) [48–52]. The HOTIs thus have broadened our understanding on topological insulating phases of matter.

There are two important excitations in magnetic systems. One is the spin wave (or magnon) [53, 54], i.e., the collective motion of magnetic moments. The topological phase of magnons in magnetic materials is of great current interest in magnetism because of its fundamental significance as well as in spintronics because of its practical utility for robust information processing [20, 22, 55–60]. The other one is the collective oscillation of magnetic solitons (such as the magnetic vortex [61, 62], bubble [63–65], skyrmion [66, 67], and domain wall [68–70]), which are long-term topic in condensed matter physics for their interesting dynamics and promising application. These magnetic solitons generally have the characteristics of small size, easy manipulation and high stability. The spintronic devices based on magnetic solitons thus have advantages over other electronic devices. For example, the racetrack memory made of magnetic domain walls can greatly improve the data storage density and the reading speed [71, 72]; the critical current density required for encoding information can be significantly reduced by using the skyrmion as the carrier of information [73, 74]; the magnetic oscillators based on vortices or skyrmions are very robust and flexible [75–77]. On the other hand, it has been shown that the collective gyration motion of magnetic solitons can exhibits the behavior of waves [78–82]. Furthermore, the first-order topological chiral edge states based on two-dimensional honeycomb lattices of magnetic solitons (vortices and bubbles) have been predicted by Kim and Tserkovnyak [83]. In a word, the metamaterials based on topological spin texture are attracting more and more attention for both fundamental interest and the potential applications in spintronics and quantum computing [84–89].

In this chapter, we report the realization of TIs in magnetic soliton lattices. The exposition is organized as follows: Sect. 15.2 introduces the topological structures, properties, and applications of magnetic solitons; the first-order topological edge states of skyrmion lattice are discussed in Sects. 15.3, 15.4 and 15.5 focus on the second-order TIs in the breathing kagome and honeycomb lattices of magnetic vortices, respectively. We summarise the results in Sect. 15.6.

15.2 Topological Structures, Properties, and Applications of Magnetic Solitons

Topology is a study of geometry or space which can keep some properties invariant under a continuous transformation. Topological magnetic soliton is an application of topology in condensed matter physics. More precisely, magnetic solitons are the spin textures characterized by a topological charge [83],

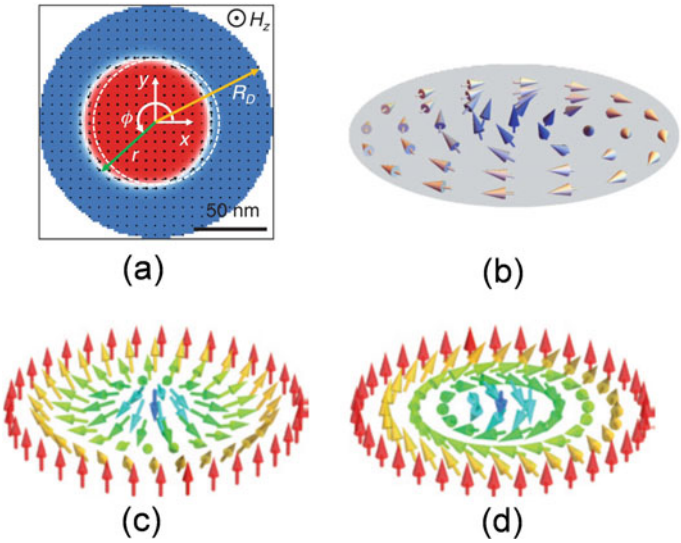

Fig. 15.1 The micromagnetic structures of magnetic bubble (**a**), vortex (**b**), Néel-type skyrmion (**c**), and Bloch-type skyrmion (**d**). Images are taken from [64, 83, 90]

$$Q = \frac{1}{4\pi} \iint dxdy\mathbf{m} \cdot (\frac{\partial \mathbf{m}}{\partial x} \times \frac{\partial \mathbf{m}}{\partial y}), \tag{15.1}$$

which counts how many times the local magnetization **m** wraps the unit sphere. Typical magnetic solitons include magnetic bubble, vortex, and skyrmion, with the micromagnetic structures shown in Fig. 15.1, respectively. The topological charge of magnetic bubble and skyrmion are ± 1, while this value changes to $\pm 1/2$ for vortex configuration. Topological charge is a topological invariant which indicates the trivial structure (for example, ferromagnetic state) can not continuously deformed into a topological spin texture because of the topological protection and the magnetic solitons with the same topological charge are homotopic.

The low-energy dynamics of the magnetic vortex can be described by the massless Thiele's equation [83, 91] whithin the approximation of the rigid model:

$$G\hat{z} \times \frac{d\mathbf{U}_j}{dt} - \alpha D \frac{d\mathbf{U}_j}{dt} + \mathbf{F}_j = 0, \tag{15.2}$$

where $\mathbf{U}_j \equiv \mathbf{R}_j - \mathbf{R}_j^0$ is the displacement of the vortex core from its equilibrium position $\mathbf{R}_j^0$; $G = -4\pi Q d M_s/\gamma$ is the gyroscopic constant with Q is the topological charge; d is the thickness of ferromagnetic layer; M_s is the saturation magnetization; γ is the gyromagnetic ratio. αD is the viscous coefficient with α being the Gilbert damping constant. The conservative force $\mathbf{F}_j = -\partial W/\partial \mathbf{U}_j$ where W is the potential energy of the system. For a single vortex, the potential energy have the parabolic type: $W = W_0 + K\mathbf{U}_j^2/2$, where W_0 is the energy of system when vortex core located at the

center of the nanodisk and K is the spring constant. By neglecting the viscous force term, we can derive the gyration frequency of an isolated vortex with $\omega_0 = K/|G|$.

However, it is well known that magnetic bubbles and skyrmions in particular manifest an inertia in their gyration motion [63, 92]. The mass effect thus should be taken into account for describing the skyrmion (or bubble) oscillation. Therefore, the Thiele's equation can be generalized as:

$$-M\frac{d^2\mathbf{U}_j}{dt^2} + G\hat{z} \times \frac{d\mathbf{U}_j}{dt} - \alpha D\frac{d\mathbf{U}_j}{dt} + \mathbf{F}_j = 0, \tag{15.3}$$

with M being the inertial mass of magnetic soliton. Similarly, we can calculate the gyration frequency of skyrmion (or bubble) with:

$$\omega_{\pm} = -G/2M \pm \sqrt{(G/2M)^2 + K/M}. \tag{15.4}$$

The positive and negative values of the ω in (15.4) indicate that there are two kinds of gyration modes with clockwise and counterclockwise direction, respectively.

Magnetic skyrmions are typical magnetic solitons stabilized by Dzyaloshinskii Moriya interactions (DMIs) [66, 93, 94]. They can be manipulated by spin-polarized electrical current with extremely low density [73, 74]. Skyrmion also can be drived by other external force, such as spin wave [95, 96], microwave field [97, 98], and temperature gradient [99–101]. Interestingly, very recently, it has been proposed that twisted photons [102] and magnons [103] carrying orbital angular momentum (OAM) can act as "optical tweezers" and "magnetic tweezers" to drive the rotation of skyrmion, as shown in Fig. 15.2 and Fig. 15.3, respectively. Theoretical calculation and numerical simulation show that the topological charge of twisted photons (or magnons) can determine both the magnitude and the handedness of the rotation velocity of skyrmions.

Skyrmions are the ideal information carrier in spintronic devices. However, a skyrmion can not move in a straight line along the driving current direction because of the Magnus force which leads to the shift of its motion trajectory, such behavior is called skyrmion Hall effect (SHE) [104, 105]. In practical applications, the skyrmion may be destroyed when touching the device boundaries. To overcome this issue, a lot of methods have been proposed. For example, X. Zhang et al. [106] showed that the antiferromagnetically exchange-coupled bilayer system containing two skyrmions with different polarities can suppress the SHE, leading to a perfectly straight trajectory for skyrmion driven by a spin-polarized current. Moreover, the antiferromagnetic (AFM) skyrmion can also avoid SHE [107, 108]. Interestingly, recent research shows that the AFM skyrmion can emerge in a ferromagnet with gain (negative α) [109]. Figure 15.4 shows the dynamical process of the formation of AFM skyrmion in ferromagnet (here α is set to be -0.01), with the initial magnetization profile being random [see Fig. 15.4a]. At $t = 0.035$ ns, local magnetic moments quickly evolve to an antiparallelly aligned state, as shown in Fig. 15.4b. Then, all spins inside a circle of radius 5 nm in the film center are randomized. At $t = 0.14$ ns, an AFM skyrmion is stabilized (see Fig. 15.4d). When an in-plane spin-polarized electric current was

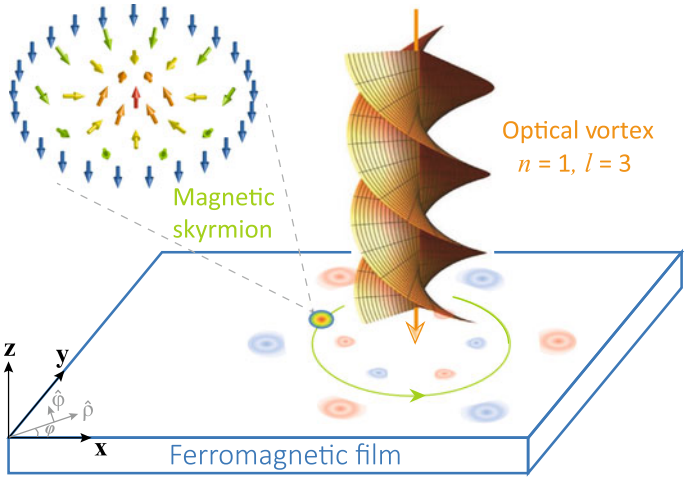

Fig. 15.2 Schematic diagram of the rotational motion of a Néel-type skyrmion in a thin ferromagnetic film driven by an optical vortex with radial index $n = 1$ and OAM quantum number $l = 3$. The solid circle with a red core represents the skyrmion. The flower-like pattern (pink and blue spots) sketches the induced magnetization profile by the optical vortex field shinning on the magnetic film. Images are taken from [102]

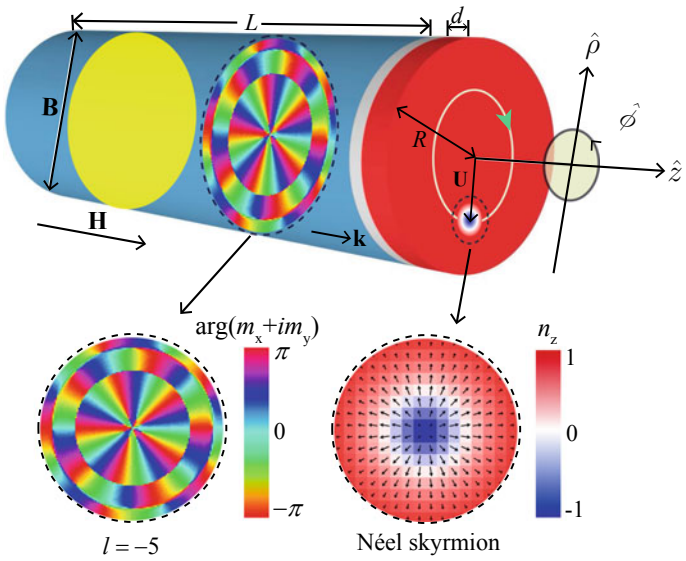

Fig. 15.3 Schematic illustration of a heterostructured nanocylinder exchange-coupled to a chiral magnetic nanodisk hosting a Néel-type skyrmion. An external static field **H** is applied along the z-direction. A spin-wave beam with the wavevector **k** and OAM quantum number $l = -5$ is excited by a localized microwave field **B**, leading to a steady skyrmion gyration around the disk center. Images are taken from [103]

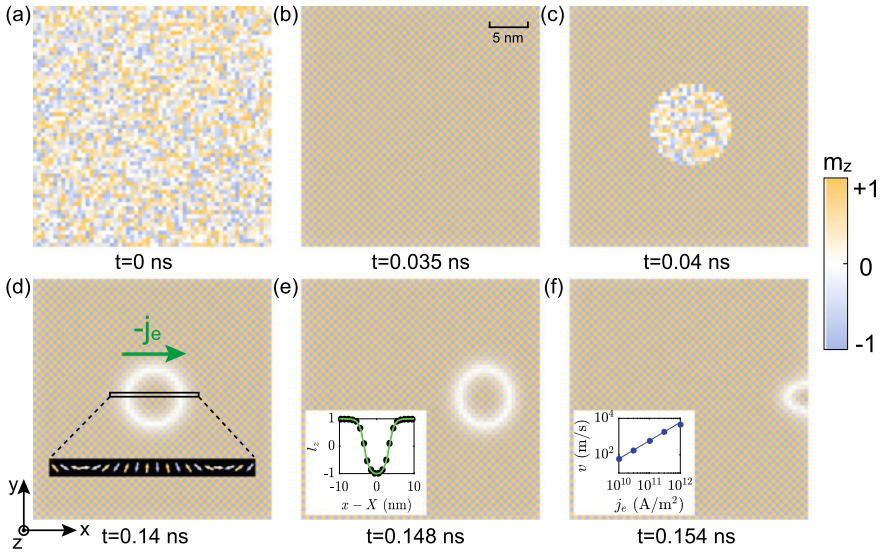

Fig. 15.4 **a** Random spin configuration at $t = 0$ ns. **b** AFM state evolved at $t = 0.035$ ns. **c** Randomizing spins inside the circle at $t = 0.04$ ns. **d** AFM skyrmion stabilized at $t = 0.14$ ns. (Inset) Magnetization profile of the cross section of the AFM skyrmion. **e** Current-driven AFM skyrmion motion. (Inset) Spatial distribution of the z component of the Néel vector $\mathbf{l}_i$. **f** AFM skyrmion annihilation at the film boundary. (Inset) Current dependence of the skyrmion velocity when it is far from the edge. Images are taken from [109]

applied to drive the AFM skyrmion, the skyrmion trajectory is exactly along the flowing direction of electrons, without the SHE. Besides, the method for the current-driven skyrmion motion on magnetic nanotubes [110] can also make the skyrmion away from the edge of system (avoid touching the edges of system), since the tube is edgeless for the tangential skyrmion motion. A stable skyrmion propagation can survive in the presence of a very large current density without any annihilation or accumulation. The nanotube can be viewed as a seamless, hollow tubular structure rolled from a planar strip, as illustrated in Fig. 15.5.

On the other hand, the magnetic skyrmions can be used to realize logical operation and thus have great potential application in logic devices [111–113]. Figure 15.6 shows typical double-track logic AND gate and OR gate based on twisted skyrmions [114]. The logical AND operation can be realized through the following processes (Fig. 15.7a1–a5): two $p = -1$ skyrmions (encoding 1) are placed at the left and right sides of the logic AND gate at $t = 0$. Here p represents the polarity of the skyrmion core. Then, driven by an electric current, the two skyrmions begin to move close to each other and become two twisted skyrmions, as shown in Fig. 15.7a2. Next, the two twisted skyrmions move along the AFM boundaries and merge into one twisted skyrmion at the intersection of the two boundaries, see Fig. 15.7a3, a4. Finally, the twisted skyrmion is pushed out of the boundary.

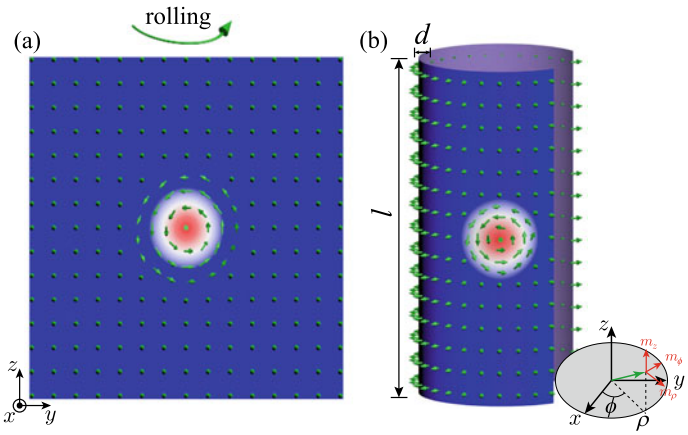

Fig. 15.5 **a** Schematic illustration of a Bloch-type skyrmion in a planar film. Green arrows refer to the local spin directions. **b** Skyrmion on a nanotube by rolling up (**a**). Colors refer to the ρ-component of the magnetization. The coordinate system is defined in the inset. Images are taken from [110]

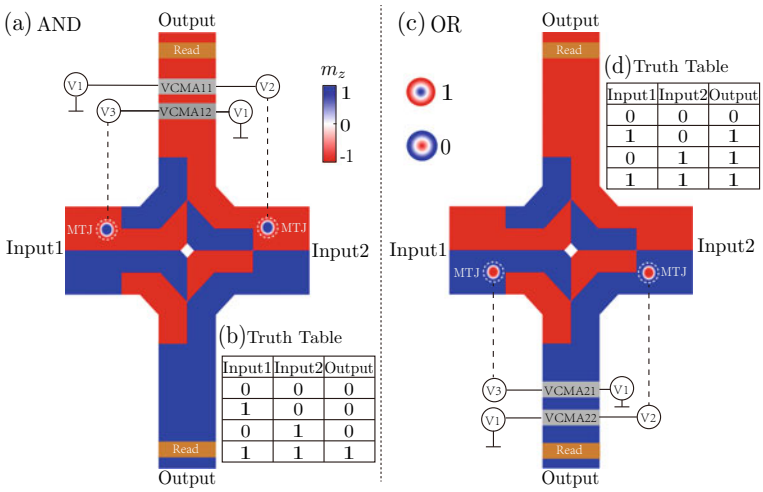

Input1	Input2	Output
0	0	0
1	0	0
0	1	0
1	1	1

Input1	Input2	Output
0	0	0
1	0	1
0	1	1
1	1	1

Fig. 15.6 Schematic plot of a logic AND (**a**) and OR (**c**) gate with two input skyrmions (top view). Truth table for the logic AND (**b**) and OR (**d**) gate. Images are taken from [114]

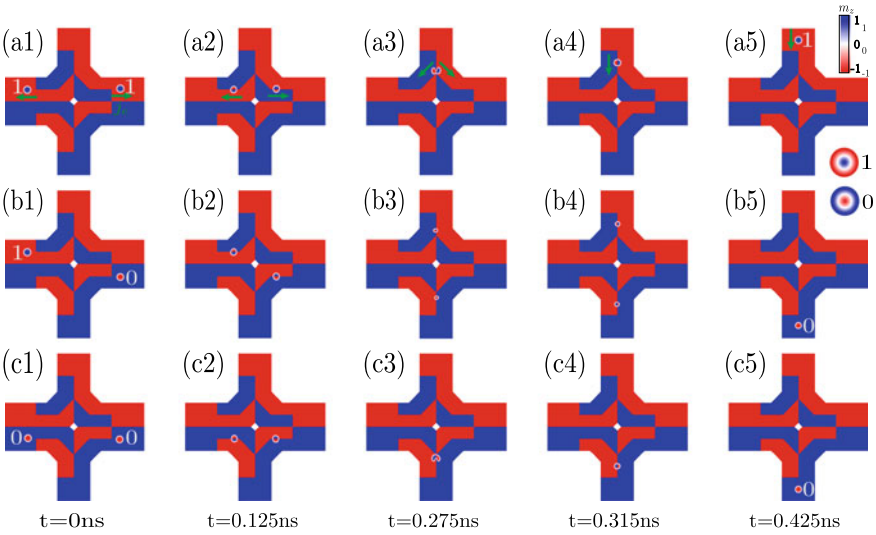

Fig. 15.7 Snapshots of the working process of skyrmions logic AND gate (top view). **a1–a5** Logic operation "1 + 1 = 1". **b1–b5** "1 + 0 = 0". **c1–c5** "0 + 0 = 0". Images are taken from [114]

Consequently, the final state is a skyrmion with $p = -1$ (encoding 1) such that "1 + 1 = 1", as shown in Fig. 15.7a5. Likewise, the other logical AND operations ("0 + 1 = 0" and "0 + 0 = 0") are plotted in Fig. 15.7b1–b5 and c1–c5, respectively.

15.3 The Topological Properties of Skyrmion Lattice

As mentioned in Sect. 15.1, Kim and Tserkovnyak have predicted theoretically the chiral edge modes in two-dimensional honeycomb lattice of vortices and bubbles by solving massless Thiele's equation [83]. However, the higher-order terms are important for describing the skyrmions (or bubbles) oscillation. In this section, we will discuss the edge states of honeycomb lattice of massive magnetic skyrmions for considering both a second-order inertial term of skyrmion mass and a third-order non-Newtonian gyroscopic term.

15.3.1 Large-Scale Micromagnetic Simulations

A large two-dimensional honeycomb lattice consisting of 984 identical magnetic nanodisks is considered to show the chiral edge states of magnetic soliton system. Figure 15.8a shows the sketch. Each disk contains a single magnetic skyrmion made of MnSi [115] which supports the Bloch-type skyrmion (depicted in Fig. 15.8b) due

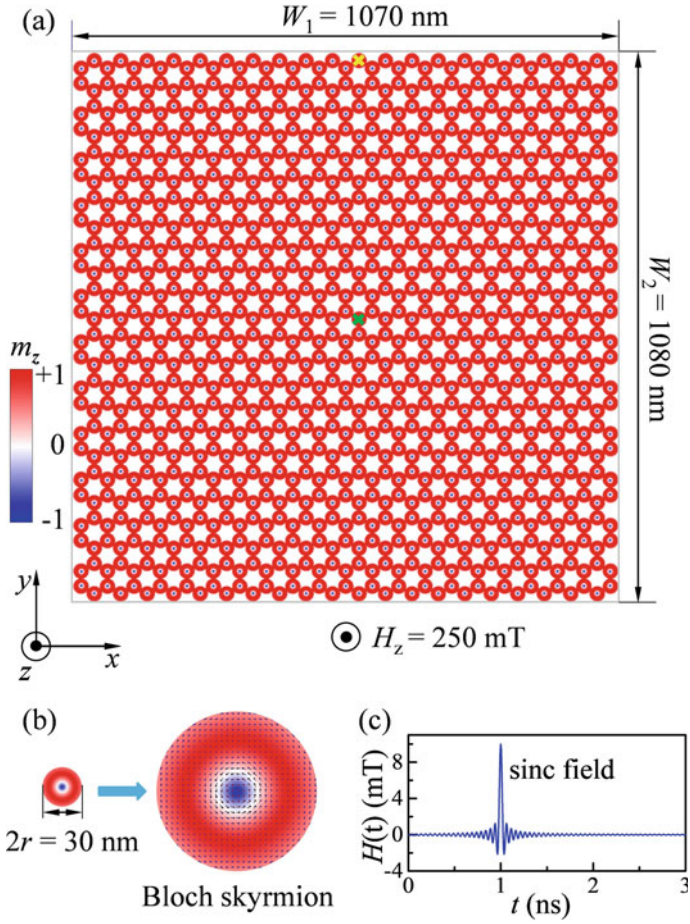

Fig. 15.8 **a** Illustration of the honeycomb lattice with size 1070 × 1080 nm^2, including 984 Bloch-type skyrmions. A uniform magnetic field is applied along the z axis to stabilize the skyrmions. Green and yellow crosses denote the positions of the driving fields in the center and at the edge of the lattice, respectively. **b** Zoomed in details of a nanodisk containing a Bloch-type skyrmion. **c** Time-dependence of the sinc-function field $H(t)$. Images are taken from [125]

to the bulk Dzyakoshinskii-Moriya interaction (DMI) [93, 116]. Here, the distance between nearest-neighbor disks is chosen to be equal to the disk diameter, indicating that nearest-neighbor skyrmions can strongly interact with each other mediated by the exchange spin-wave. It is worth noting that the dipolar interaction can not efficiently couple skyrmions when a physical gap between nearest-neighboring nanodisks is left. The micromagnetic simulations are performed with MUMAX3 [117].

The dispersion relation of skyrmion gyrations can be obtained by computing the spatiotemporal Fourier spectrum of the skyrmion positions over the lattice. Figure 15.9a shows the simulated band structure of skyrmion oscillation below a

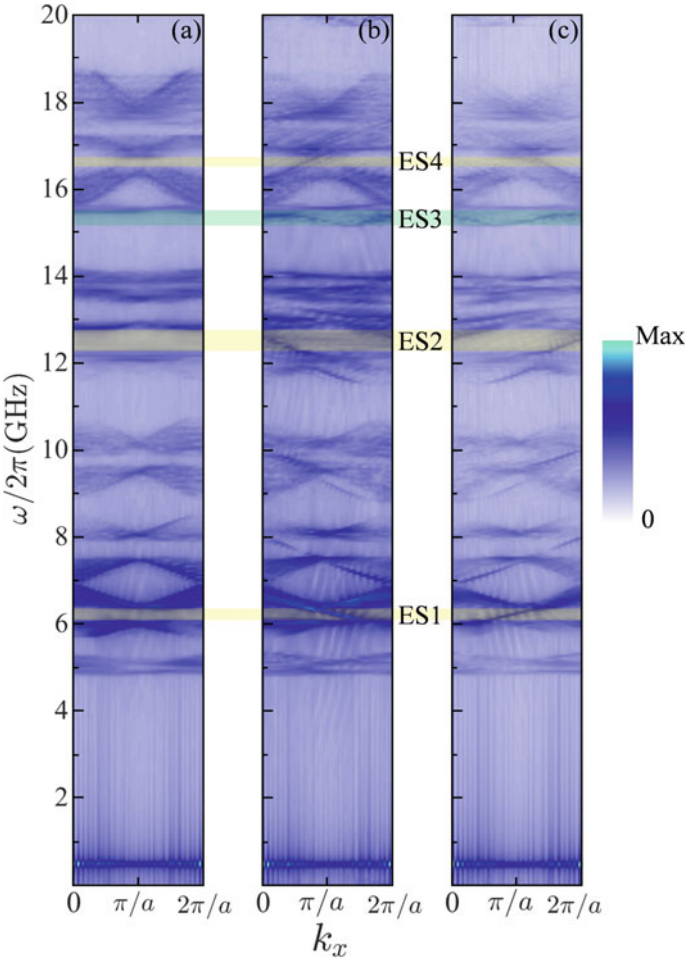

Fig. 15.9 The band structure of skyrmion gyrations when the exciting field is in the film center **a** and at the film edge by evaluating the Fourier spectrum over the upper **b** and the lower **c** parts of the honeycomb lattice. The constant $a = 2\sqrt{3}r$ represents the distance between the second-nearest neighboring nanodisks. Images are taken from [125]

cutoff frequency of 20 GHz when the exciting field (sinc-function magnetic field) locates in the lattice center. It can be seen that there is no bulk state in the gaps (areas shaded in both yellow and green). However, when the driving field is located at the edge of lattice, the situations are totally different. By implementing the Fourier analysis over the upper ($W_2/2 < y < W_2$) and the lower parts ($0 < y < W_2/2$) of the lattice, with results plotted in Fig. 15.9b, c, respectively, one can find that four edge states emerge in the spectrum gaps, labeled as ES1–ES4. Moreover, By evaluating the group velocity $d\omega/dk_x$ of each mode with ω the frequency and k_x the wave vector

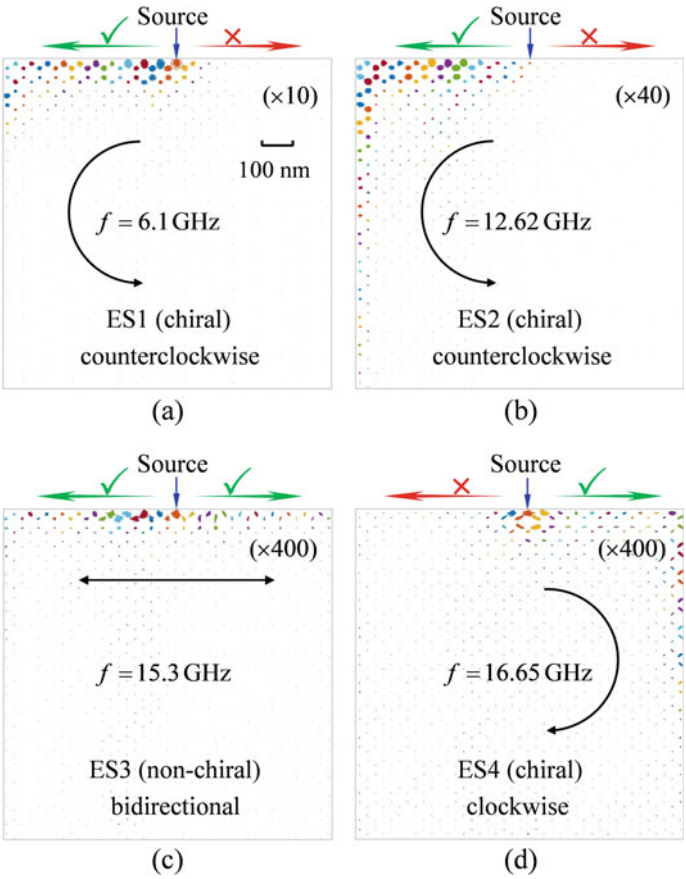

Fig. 15.10 Snapshot of the propagation of edge states with frequency $f = 6.1$ GHz (**a**), 12.62 GHz (**b**), 15.3 GHz (**c**), and 16.65 GHz (**d**) at $t = 40$ ns. Since the oscillation amplitudes of the skyrmion guiding centers are too small, we have magnified them by 10, 40 or 400 times labeled in each figure, correspondingly. Images are taken from [125]

along x direction, the chirality of these edge states can be identified: three edge states ES1, ES2 and ES4 (shaded in yellow) are unidirectional and chiral, in which ES1 and ES2 counterclockwise propagate, while ES4 behaves oppositely; ES3 (shaded in green) is bidirectional and thus non-chiral.

We choose four representative frequencies to visualize the propagation of edge wave by stimulating the dynamics of lattice under a sinusoidal field $\mathbf{h}(t) = h_0 \sin(2\pi f t)\hat{x}$ on one disk at the top edge, indicated by the blue arrows in Fig. 15.10. Figures 15.10a, b, d show the propagation of chiral edge states. One can clearly observe unidirectional wave propagation of these modes with either a counterclockwise manner (ES1 and ES2 shown in Fig. 15.10a, b respectively) or a clockwise one (ES4 plotted in Fig. 15.10d). It's very interesting and unique that multiband edge

states with opposite chiralities coexist in a given soliton lattice. There is no analogue in condensed matter system, to the best of our knowledge. In contrast, the propagation of ES3 is bidirectional, as shown in Fig. 15.10c. This non-chiral mode can be simply explained in terms of the Tamm-Shockley mechanism [118, 119] which predicts that the periodicity breaking of the crystal potential at the boundary can lead to the formation of a conducting surface/edge state. Furthermore, it is rather straightforward to show the propagation of the chiral modes is immune from the defects and robust against the type of boundary, while the Tamm-Shockley mode is not.

15.3.2 Theoretical Model

We adopt the generalized Thiele's equation to theoretically understand the multiband chiral skyrmionic edge states carrying opposite chiralities. First of all, we assume that the steady-state magnetization $\mathbf{m}$ depends on not only the position of the guiding center $\mathbf{R}(t)$ but also its velocity $\dot{\mathbf{R}}(t)$ and acceleration $\ddot{\mathbf{R}}(t)$, and write $\mathbf{m} = \mathbf{m}(\mathbf{r} - \mathbf{R}(t), \dot{\mathbf{R}}(t), \ddot{\mathbf{R}}(t))$. After some algebra and by neglecting the damping term, one can obtain the generalized Thiele's equation including both a second-order inertial term of skyrmion mass M [63, 92, 102] and a non-Newtonian third-order gyroscopic term G_3 [120–122]:

$$G_3\hat{z} \times \frac{d^3\mathbf{U}_j}{dt^3} - M\frac{d^2\mathbf{U}_j}{dt^2} + G\hat{z} \times \frac{d\mathbf{U}_j}{dt} + \mathbf{F}_j = 0, \tag{15.5}$$

where $\mathbf{U}_j$ and G share the same definition as (15.2). The conservative force can be expressed as $\mathbf{F}_j = -\partial W/\partial \mathbf{U}_j$. Here W is the total potential energy for the sum of single disk and the interaction energy between nearest-neighbor disks: $W = \sum_j K\mathbf{U}_j^2/2 + \sum_{j\neq k} U_{jk}/2$ with $U_{jk} = I_\parallel U_j^\parallel U_k^\parallel - I_\perp U_j^\perp U_k^\perp$ [83, 123, 124]. $I_\parallel$ and $I_\perp$ are the longitudinal and the transverse coupling constants, respectively. By imposing $\mathbf{U}_j = (u_j, v_j)$ and defining $\psi_j = u_j + iv_j$, we have:

$$\hat{\mathcal{D}}\psi_j = \omega_K\psi_j + \sum_{k\in\langle j\rangle}(\zeta\psi_k + \xi e^{i2\theta_{jk}}\psi_k^*), \tag{15.6}$$

where the differential operator $\hat{\mathcal{D}} = i\omega_3\frac{d^3}{dt^3} - \omega_M\frac{d^2}{dt^2} + i\frac{d}{dt}$, $\omega_3 = G_3/|G|$, $\omega_M = M/|G|, \omega_K = K/|G|, \zeta = (I_\parallel - I_\perp)/2|G|$, and $\xi = (I_\parallel + I_\perp)/2|G|, \theta_{jk}$ is the angle of the direction $\hat{e}_{jk}$ from x axis with $\hat{e}_{jk} = (\mathbf{R}_k^0 - \mathbf{R}_j^0)/|\mathbf{R}_k^0 - \mathbf{R}_j^0|$, and $\langle j\rangle$ is the set of the nearest neighbors of j (here $Q = -1$). We then expand the complex variable to

$$\psi_j = \chi_j(t)\exp(-i\omega_0 t) + \eta_j(t)\exp(i\omega_0 t). \tag{15.7}$$

For counterclockwise (clockwise) skyrmion gyrations, one can justify $|\chi_j| \gg |\eta_j|$ ($|\chi_j| \ll |\eta_j|$). Substituting (15.7) into (15.6), one can obtain the following eigenvalue equation:

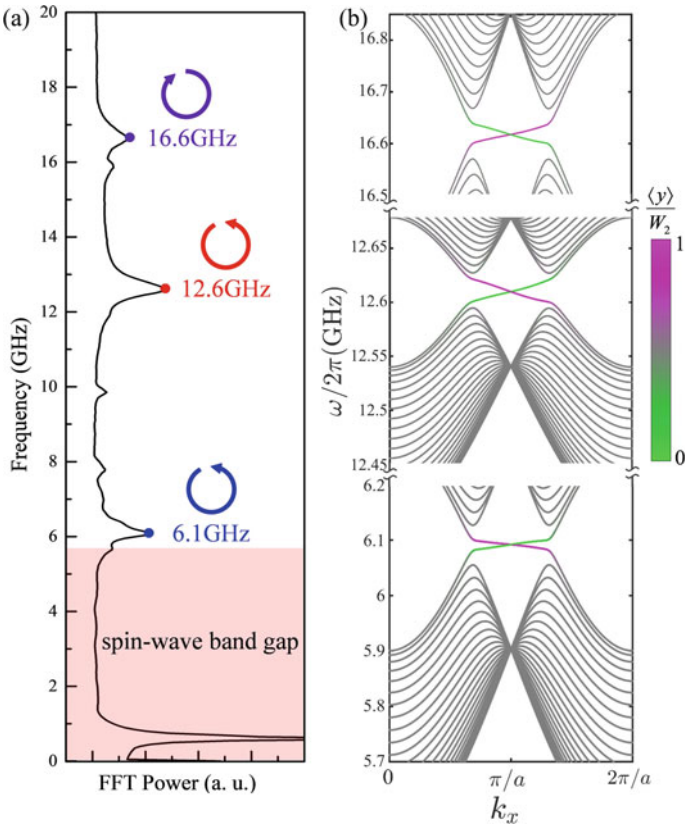

Fig. 15.11 **a** Resonant spectrum of skyrmion gyrations when the exciting field is applied over the whole system. Inset shows the chirality/handedness of the skyrmion guiding center of each mode. **b** Band structure by solving (15.8). Images are taken from [125]

$$\hat{\mathcal{D}}\psi_j = (\omega_K - 3\xi^2/2\bar{\omega}_K)\psi_j + \zeta \sum_{k\in\langle j\rangle} \psi_k - (\xi^2/2\bar{\omega}_K) \sum_{l\in\langle\langle j\rangle\rangle} e^{i2\bar{\theta}_{jl}}\psi_l, \qquad (15.8)$$

with $\bar{\omega}_K = \omega_K - \omega_0^2\omega_M$, $\bar{\theta}_{jl} = \theta_{jk} - \theta_{kl}$ the relative angle from the bond $k \to l$ to the bond $j \to k$ with k between j and l, and $\langle\langle j\rangle\rangle$ the set of the second-nearest neighbors of j.

The key parameters G_3, M, K, $I_\parallel$ and $I_\perp$ can be determined from micromagnetic simulations in a self-consistent manner [125]. Figure 15.11a shows the spectrum of collective skyrmion oscillations with three strong resonance peaks at $\omega_{0,1}/2\pi = 6.1$ GHz, $\omega_{0,2}/2\pi = 12.6$ GHz, and $\omega_{0,3}/2\pi = 16.6$ GHz above the spin-wave band gap. Furthermore, Fig. 15.11b shows the computed band structure of the skyrmion gyrations near the resonance frequencies $\omega_0 = \omega_{0,1}$, $\omega_{0,2}$, and $\omega_{0,3}$ by solving (15.8) with the periodic boundary condition along x direction and the

zigzag termination at $y = 0$ and $y = W_2$. The average vertical position of the modes $\langle y \rangle \equiv \sum_j R^0_{j,y} |\mathbf{U}_j|^2 / \sum_j |\mathbf{U}_j|^2$ are also shown in Fig. 15.11, where $R^0_{j,y}$ is the equilibrium position of the skyrmion projected onto the y axis, represented by different colors: closer to magenta indicating more localized at the upper edge. It is interesting to note that the chirality of ES4 is opposite to those of ES1 and ES2. An interpretation is as following: The direction reversal of the skyrmion gyration generates a π phase accumulation in the next-nearest-neighbor hopping term of (15.8). The Chern numbers of two neighbouring bulk bands then switch their signs, so that the chirality of the edge state in between reverses.

15.4 Corner States in a Breathing Kagome Lattice of Vortices

In previous sections, we have discussed the topological insulating phases in magnetic system. All these phases, however, are first order by nature. In this section, we will discuss the higher-order topological edge states (corner states) in magnetic system, and demonstrate their features in breathing kagome lattice of magnetic vortices.

15.4.1 The Theoretical Results and Discussions

A breathing kagome lattice of magnetic nanodisks with vortex states is considered. Figure 15.12a plots the lattice structure with alternate distance parameters d_1 and d_2. We start with the generalized Thiele's equation (15.6) to describe the collective dynamics of vortex lattice:

$$\hat{\mathcal{D}}\psi_j = \omega_K \psi_j + \sum_{k \in \langle j \rangle, l} (\zeta_l \psi_k + \xi_l e^{i2\theta_{jk}} \psi_k^*), \tag{15.9}$$

where the differential operator $\hat{\mathcal{D}} = i\omega_3 \frac{d^3}{dt^3} - \omega_M \frac{d^2}{dt^2} - i\frac{d}{dt}$, $\zeta_l = (I_{\parallel,l} - I_{\perp,l})/2|G|$, and $\xi_l = (I_{\parallel,l} + I_{\perp,l})/2|G|$, with $l = 1$ (or $l = 2$) representing the distance d_1 (or d_2) between the nearest neighbor vortices, here the topological charge $Q = 1/2$.

The coupling strengths $I_\parallel$ and $I_\perp$ are strongly depend on the parameter d ($d = d'/r$ with d' the distance between two vortices and r being the radius of nanodisk) [127–129]. The analytical expression of $I_\parallel(d)$ and $I_\perp(d)$ are essential for evaluating the spectrum and the phase diagram of vortex gyrations. With the help of micromagnetic simulations for two-vortex system with different combinations of vortex polarities, one can obtain the best fit of the numerical data: $I_\parallel = \mu_0 M_s^2 r(-1.72064 \times 10^{-4} + 4.13166 \times 10^{-2}/d^3 - 0.24639/d^5 + 1.21066/d^7 - 1.81836/d^9)$ and $I_\perp = \mu_0 M_s^2 r\,(5.43158 \times 10^{-4} - 4.34685 \times 10^{-2}/d^3 + 1.23778/d^5 - 6.48907/d^7 +$

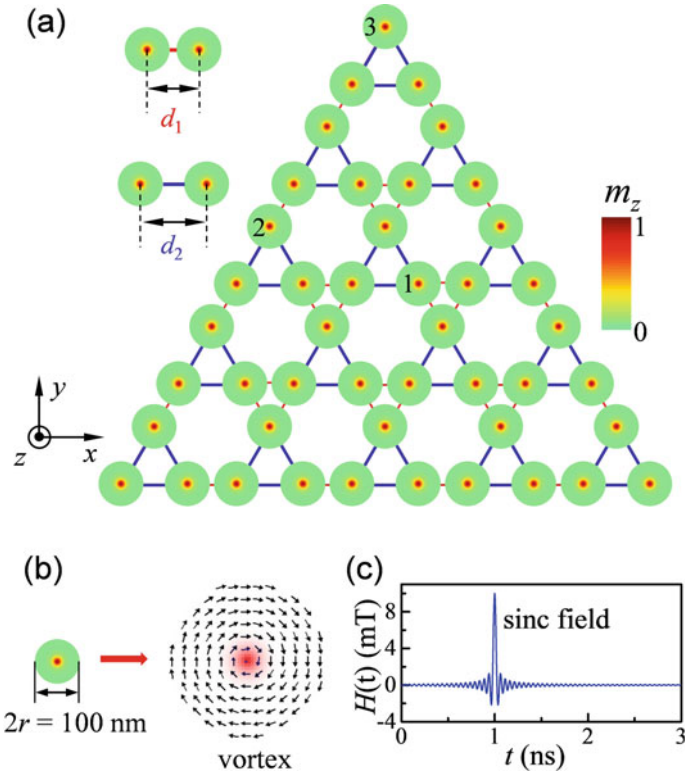

Fig. 15.12 **a** Illustration of the triangle-shape breathing kagome lattice including 45 nanodisks of the vortex state. d_1 and d_2 are the distance between two nearest-neighbor vortices. Arabic numbers 1, 2 and 3 denote the positions of spectrum analysis for bulk, edge and corner states, respectively. **b** Zoomed in details of a nanodisk with the radius $r = 50$ nm and the thickness $w = 10$ nm. **c** Time dependence of the sinc-function field $H(t)$ applied to the whole system. Images are taken from [126]

$13.6422/d^9$), as shown in Fig. 15.13a with symbols and curves representing simulation results and analytical formulas, respectively. In the calculations, the material parameters of Permalloy (Py: $Ni_{80}Fe_{20}$) [88, 130] was adopted, and $G = -3.0725 \times 10^{-13}$ J s rad^{-1}m^{-2}. The spring constant K, mass M, and non-Newtonian gyration G_3 can be obtained by analyzing the dynamics of a single vortex confined in the nanodisk [126]: $K = 1.8128 \times 10^{-3}$ J m^{-2}, $M = 9.1224 \times 10^{-25}$ kg, and $G_3 = -4.5571 \times 10^{-35}$J s^{3}rad^{-3}m^{-2}. Then, the eigenfrequencies of vortex gyrations in the breathing kagome lattice can be obtained by solving (15.9) numerically. Figure 15.13b shows the eigenfrequencies of the triangle-shape system for different values d_2/d_1 with a fixed $d_1 = 2.2r$. The results of the spatial distribution of the corresponding eigenfunctions show that corner states can exist only if $d_2/d_1 > 1.2$, as indicated by the red line segment. Different choices of d_1 gives almost the same conclusion. Furthermore, the complete phase diagram can be calculated by sys-

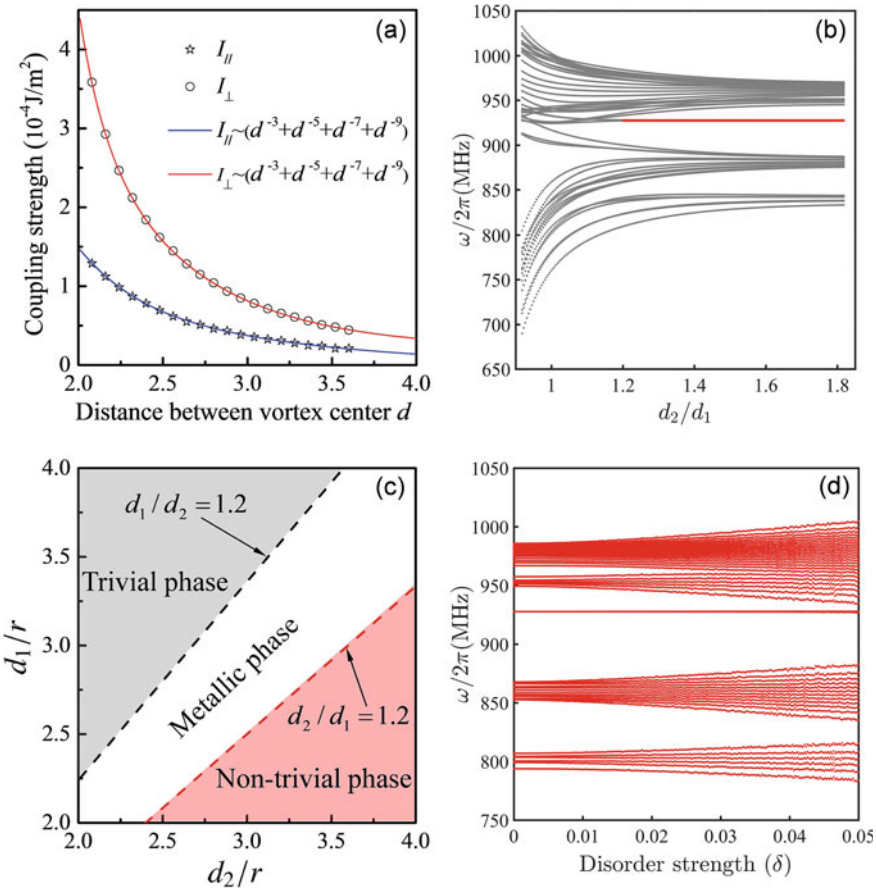

Fig. 15.13 **a** Dependence of the coupling strength $I_{\parallel}$ and $I_{\perp}$ on the vortex-vortex distance d (normalized by the disk radius r). Pentagrams and circles denote simulation results and solid curves represent the analytical fitting. **b** Eigenfrequencies of collective vortex gyration under different ratio d_2/d_1 with the red segment labeling the corner state phase. **c** The phase diagram. **d** Eigenfrequencies of the breathing kagome lattice of vortices under different disorder strength. Images are taken from [126]

tematically changing d_1 and d_2. It can be clearly seen that the boundary separating topologically non-trivial and metallic phases lies in $d_2/d_1 = 1.2$, while topologically trivial and metallic phases are separated by $d_1/d_2 = 1.2$, as shown in Fig. 15.13c. When $d_2/d_1 > 1.2$, the system is topologically non-trivial and can support second-order topological corner states. The system is trivial without any topological edge modes if $d_1/d_2 > 1.2$. Here, the trivial phase is the gapped (insulator) state, the metallic/conducting phase represents the gapless state such that vortices oscillations can propagate in the bulk lattice, and the non-trivial phase means the second-order corner state surviving in a gapped bulk. Besides, it is worth mentioning that the critical

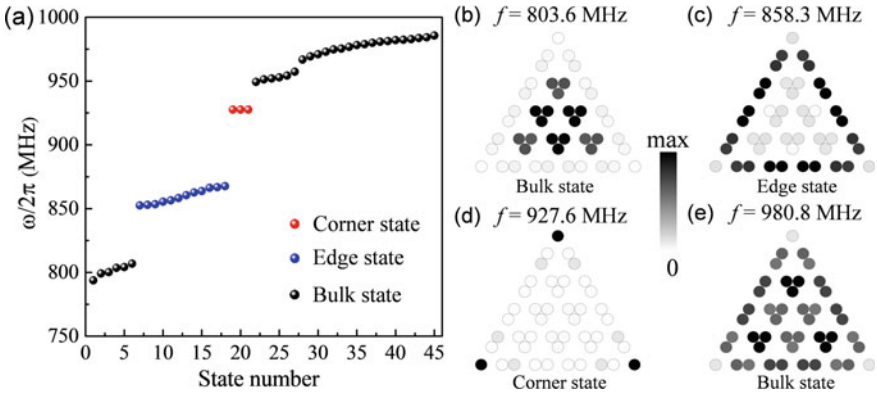

Fig. 15.14 **a** Eigenfrequencies of triangle-shape kagome vortex lattice with $d_1 = 2.08r$ and $d_2 = 3.60r$. The spatial distribution of vortex gyrations for the bulk [(**b**) and (**e**)], edge (**c**), and corner (**d**) states. Images are taken from [126]

condition ($d_2/d_1 > 1.2$) for HOTIs may vary with respect to materials parameters. For example, the critical value will slightly increase (decrease) if the radius of the nanodisk increases (decreases).

Topological corner states should be robust against disorders in the bulk. Figure 15.13d shows the eigenfrequencies of the triangle-shape breathing kagome lattice of vortices under bulk disorders of different strengths, where $d_1 = 2.08r$ and $d_2 = 3.60r$ ($d_2/d_1 = 1.73 > 1.2$). Here, disorders are introduced by assuming the resonant frequency ω_0 with a random shift, i.e., $\omega_0 \to \omega_0 + \delta Z \omega_0$, where δ indicates the strength of the disorder and Z is a uniformly distributed random number between -1 to 1. It can be seen from Fig. 15.13d that with the increasing of the disorder strength, the spectrum of both edge and bulk states is significantly modified, while the corner states are quite robust. What's more, it can be further confirmed that these corner states are also robust against defects.

The same geometric parameters as Fig. 15.13d are chosen to explicitly visualize the corner states and other modes in the phase diagram. The computed eigenfrequencies and eigenmodes are plotted in Fig. 15.14a–e, respectively. It is found that there are three degenerate modes with the frequency equal to 927.6 MHz, represented by red balls. These modes are indeed second-order topological states (corner states) with oscillations being highly localized at the three corners, see Fig. 15.14d. The edge states are also identified, denoted by blue balls in Fig. 15.14a. The spatial distribution of edge oscillations are confined on three edges, as shown in Fig. 15.14c. However, these edge modes are Tamm-Shockley type [118, 119], not chiral, which can be confirmed by micromagnetic simulations [126]. Bulk modes are plotted in Fig. 15.14b, e, where corners do not participate in the oscillations.

The higher-order topological properties can be interpreted in terms of the bulk topological index, i.e., the polarization [131, 132]:

$$P_j = \frac{1}{S} \iint_{\mathrm{BZ}} A_j d^2k, \tag{15.10}$$

where S is the area of the first Brillouin zone, $A_j = -i\langle\psi|\partial k_j|\psi\rangle$ is Berry connection with $j = x, y$, and ψ is the wave function for the lowest band. It is shown that $(P_x, P_y) = (0.499, 0.288)$ for $d_1 = 2.08r$ and $d_2 = 3.60r$ and $(P_x, P_y) = (0.032, 0.047)$ for $d_1 = 3r$ and $d_2 = 2.1r$. The former corresponds to the topological insulating phase while the latter is for the trivial phase. Theoretically, for breathing kagome lattice, the polarization (P_x, P_y) is identical to Wannier center, which is restricted to two positions for insulating phases. If Wannier center coincides with (0, 0), the system is in trivial insulating phase and no topological edge states exist. Higher-order topological corner states emerge when the Wannier center lies at (1/2, $1/2\sqrt{3}$) [25, 36]. The distribution of bulk topological index is consistent with the computed phase diagram Fig. 15.13c.

The other type of breathing kagome lattice of vortices (parallelogram-shape) also supports the corner states, with the sketch plotted in Fig. 15.15a. Here, the same parameters as those in the triangle-shape lattice are adopted. Figure 15.15b shows the eigenfrequencies of system. Interestingly, it can be seen that there is only one corner state, represented by the red ball. Edge and bulk states are also observed, denoted by blue and black balls, respectively. The spatial distribution of vortices oscillation for different modes are shown in Fig. 15.15c–f. From Fig. 15.15e, one can clearly see that the oscillations for corner state are confined to one acute angle and the vortex at the position of two obtuse angles hardly oscillates. The spatial distribution of vortex gyration for edge and bulk states are plotted in Fig. 15.15c, d, f. Further, the robustness of the corner states are also confirmed [126].

It is interesting to note that the results of triangle-shape and parallelogram-shape lattices are closely related. Two opposite acuted-angle corners in the parallelogram are actually not equivalent: one via d_1 bonding while the other one via d_2 bonding; see Fig. 15.15a. Only the d_2 bonding (bottom-right) corner in the parallelogram-shape lattice is identical to three corners in the triangle-shape lattice. Therefore, for parallelogram-shape lattice, we can observe only one corner state.

15.4.2 Micromagnetic Simulations

Micromagnetic simulations are implemented to verify the theoretical predictions of corner states above. The breathing kagome lattice consisting of massive identical magnetic nanodisks in vortex states are considered, as shown in Figs. 15.12a and 15.15a, with the same geometric parameters as those in Figs. 15.14a and 15.15b, respectively. Micromagnetic software MUMAX3 [117] is used to simulate the dynamics of vortices.

Figure 15.16a shows the temporal Fourier spectra of the vortex oscillations at different positions, with black, blue, and red curves denoting the positions of bulk, edge, and corner bands, respectively. One can immediately see that, near the frequency of

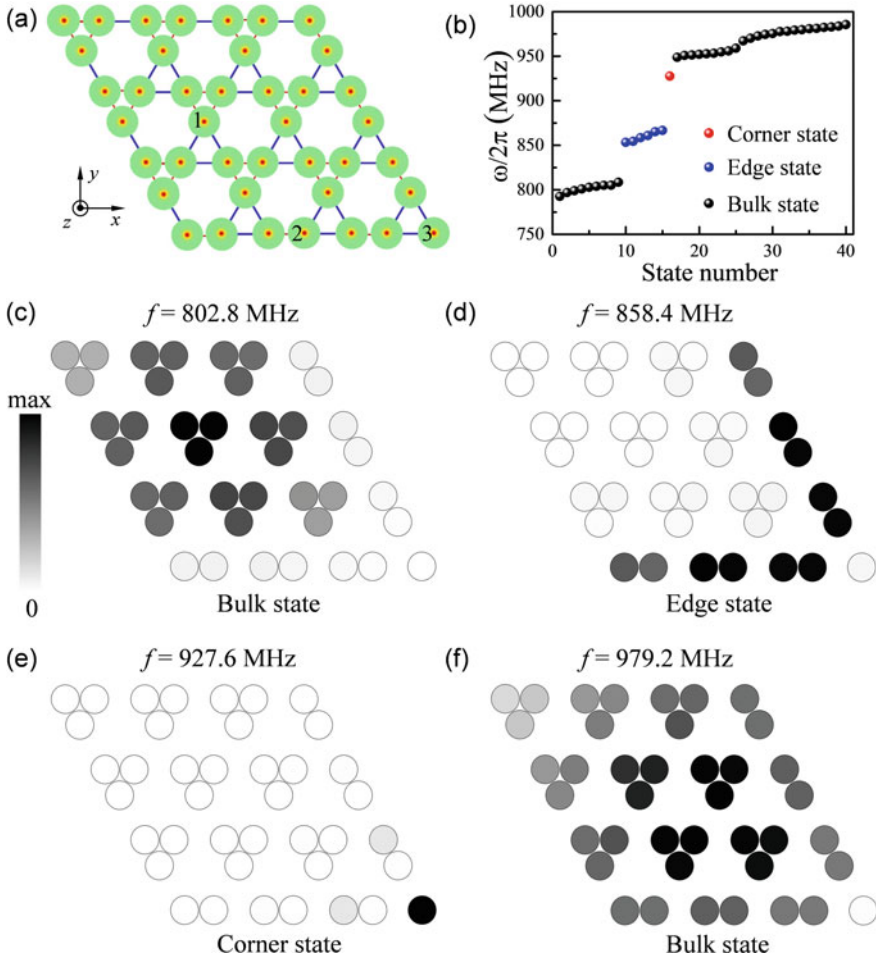

Fig. 15.15 **a** The sketch for parallelogram-shaped breathing kagome lattice of vortices. Arabic numbers 1, 2 and 3 denote the position of spectrum analysis for bulk, edge, and corner states, respectively. **b** Numerically computed eigenfrequencies for parallelogram-shaped system. The spatial distribution of vortices oscillation for the bulk [(**c**) and (**f**)], edge (**d**), and corner (**e**) states. Images are taken from [126]

940 MHz, the spectrum for the corner has a very strong peak, which does not happen for the edge and bulk. It can be inferred that this is the corner-state band with oscillations localized only at three corners. Similarly, one can identify the frequency range which allows the bulk and edge states, as shown by shaded area with different colors in Fig. 15.16a. Four representative frequencies are chosen to visualize the spatial distribution of vortex oscillations for different modes: 940 MHz for the corner state, 842 MHz for the edge state, and both 769 MHz and 959 MHz for bulk states, and then stimulate their dynamics by a sinusoidal magnetic field $\mathbf{h}(t) = h_0 \sin(2\pi f t)\hat{x}$ with

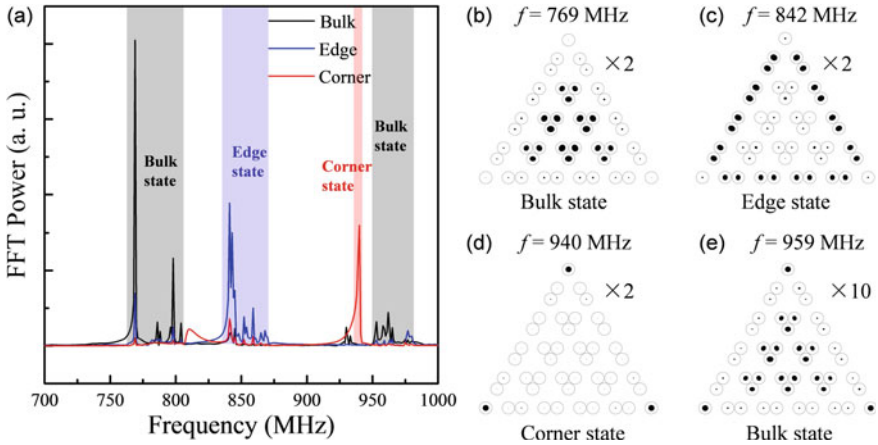

Fig. 15.16 Micromagnetic simulation of excitations in triangle-shape structure. **a** The temporal Fourier spectrum of the vortex oscillations at different positions. The spatial distribution of oscillation amplitude under the exciting field of various frequencies, 769 MHz (**b**), 842 MHz (**c**), 940 MHz (**d**), and 959 MHz (**e**). Since the oscillation amplitudes of the vortex centers are too small, we have magnified them by 2 or 10 times labeled in each figure. Images are taken from [126]

$h_0 = 0.1$ mT to the whole system for 100 ns. Figures 15.16b–e plot the spatial distribution of oscillation amplitude. One can clearly see the corner state in Fig. 15.16d, which is in a good agreement with theoretical results shown in Fig. 15.14d. Spatial distribution of vortices motion for bulk and edge states are shown in Fig. 15.16b, c, respectively. It is worth noting that vortices at three corners in Fig. 15.16e also oscillate with a sizable amplitude, which is somewhat quite unexpected for bulk states. This inconsistency may come from the strong coupling (or hybridization) between the bulk and corner modes, since their frequencies are very close to each other, as shown in Figs. 15.14a and 15.16a.

The simulations of parallelogram-shaped lattice show similar results to triangle-shaped lattice. The spectra are shown in Fig. 15.17a with the black, blue and red curves indicating the positions of bulk (Number 1), edge (Number 2) and corner (Number 3) bands, respectively. Shaded area with different colors denote different modes. The spatial distribution of oscillation amplitude is plotted in Fig. 15.17b–e. Figure 15.17d shows only one corner state at only one (bottom-right) acute angle, which is in a good agreement with theoretical results shown in Fig. 15.15e. Spatial distribution of vortices motion for bulk and edge states are shown in Fig. 15.17b, c, respectively. Interestingly, the hybridization between bulk mode and corner mode occurs as well in parallelogram-shaped lattice, see Fig. 15.17e.

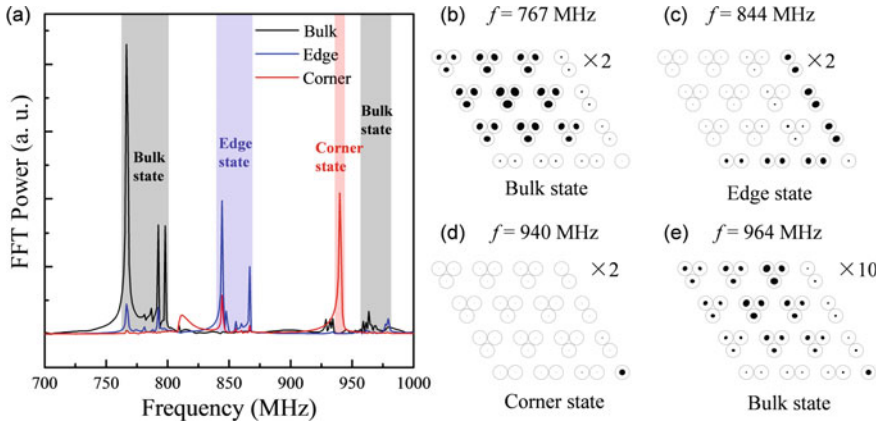

Fig. 15.17 Micromagnetic simulation of excitations in parallelogram-shape structure. **a** The temporal Fourier spectrum of the vortex oscillations at different positions. The spatial distribution of oscillation amplitude under the exciting field with different frequencies, 767 MHz (**b**), 844 MHz (**c**), 940 MHz (**d**), and 964 MHz (**e**). The simulation time is 100 ns. Since the oscillation amplitudes of the vortices centers are too small, we have magnified them by 2 or 10 times labeled in each figure. Images are taken from [126]

15.5 Corner States in a Breathing Honeycomb Lattice of Vortices

It is known that the perfect graphene lattice has a gapless band structure with Dirac cones in momentum space [133]. When spatially periodic magnetic flux [134] or spin-orbit coupling [135] are introduced, a gap opens at the Dirac point, leading to a FOTI. Interestingly, the realization of gap opening and closing by tuning the intercellular and intracellular bond distances has been demonstrated in photonic [31] and elastic [136] honeycomb lattices, in which HOTI emerges. In this section, we show that the higher-order topological insulating phase do exist in a breathing honeycomb lattice of vortices.

15.5.1 Theoretical Model

Figure 15.18 shows a breathing honeycomb lattice of magnetic nanodisks with vortex states. We use (15.9) to describe the collective dynamics of the breathing honeycomb lattice of vortices. For vortex (topological charge $Q = +1/2$) gyrations, one can justify $|\chi_j| \ll |\eta_j|$. By substituting (15.7) into (15.9), we obtain the eigenvalue equation of the system,

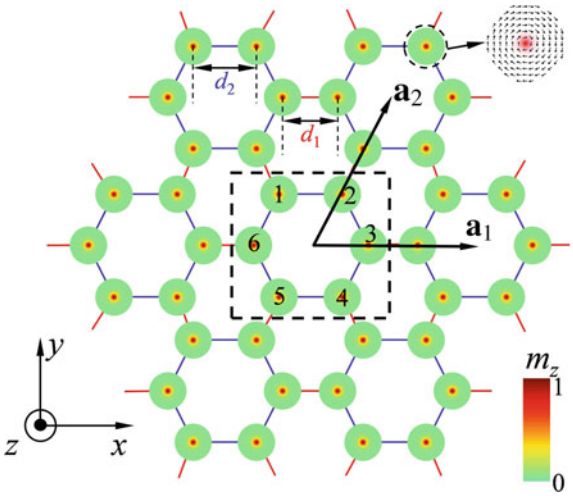

Fig. 15.18 Illustration (top view) of the breathing honeycomb lattice of magnetic vortices, with d_1 and d_2 denoting the alternating lengths of intercellular and intracellular bonds, respectively. The radius of each nanodisk is $r = 50$ nm, and the thickness is $w = 10$ nm. The dashed black rectangle is the unit cell used for calculating the band structure, with $\mathbf{a}_1$ and $\mathbf{a}_2$ denoting the basis vectors. Images are taken from [137]

$$\hat{\mathcal{D}}\psi_j = (\omega_0 - \frac{\xi_1^2 + 2\xi_2^2}{2\omega_K})\psi_j + \zeta_1 \sum_{k\in\langle j_1\rangle} \psi_k + \zeta_2 \sum_{k\in\langle j_2\rangle} \psi_k$$
$$-\frac{\xi_1\xi_2}{2\omega_K} \sum_{s\in\langle\langle j_1\rangle\rangle} e^{i2\bar{\theta}_{js}}\psi_s - \frac{\xi_2^2}{2\omega_K} \sum_{s\in\langle\langle j_2\rangle\rangle} e^{i2\bar{\theta}_{js}}\psi_s, \tag{15.11}$$

with $\omega_K = \omega_0 - \omega_0^2\omega_M$, $\bar{\theta}_{js} = \theta_{jk} - \theta_{ks}$ is the relative angle from the bond $k \to s$ to the bond $j \to k$ with k between j and s, $\langle j_1\rangle$ and $\langle j_2\rangle$ ($\langle\langle j_1\rangle\rangle$ and $\langle\langle j_2\rangle\rangle$) are the set of nearest (next-nearest) intercellular and intracellular neighbors of j, respectively.

For an infinite lattice, with the dashed black rectangle indicating the unit cell, as shown in Fig. 15.18, $\mathbf{a}_1 = a\hat{x}$ and $\mathbf{a}_2 = \frac{1}{2}a\hat{x} + \frac{\sqrt{3}}{2}a\hat{y}$ are two basis vectors of the crystal, with $a = d_1 + 2d_2$. The band structure of system can be calculated by diagonalizing the Hamiltonian,

$$\mathcal{H} = \begin{pmatrix} Q_0 & \zeta_2 & Q_1 & Q_2 & Q_3 & \zeta_2 \\ \zeta_2 & Q_0 & \zeta_2 & Q_4 & \zeta_1 \exp(i\mathbf{k}\cdot\mathbf{a}_2) & Q_5 \\ Q_1^* & \zeta_2 & Q_0 & \zeta_2 & Q_6 & \zeta_1 \exp(i\mathbf{k}\cdot\mathbf{a}_1) \\ Q_2^* & Q_4^* & \zeta_2 & Q_0 & \zeta_2 & Q_7 \\ Q_3^* & \zeta_1 \exp(-i\mathbf{k}\cdot\mathbf{a}_2) & Q_6^* & \zeta_2 & Q_0 & \zeta_2 \\ \zeta_2 & Q_5^* & \zeta_1 \exp(-i\mathbf{k}\cdot\mathbf{a}_1) & Q_7^* & \zeta_2 & Q_0 \end{pmatrix}, \tag{15.12}$$

with elements explicitly expressed as

$$
\begin{aligned}
Q_0 &= \omega_0 - \frac{\xi_1^2 + 2\xi_2^2}{2\omega_K}, \\
Q_1 &= -\frac{\xi_1\xi_2}{2\omega_K}\exp(i\frac{2\pi}{3})\Big\{\exp[i\mathbf{k}\cdot(\mathbf{a}_2-\mathbf{a}_1)] + \exp(-i\mathbf{k}\cdot\mathbf{a}_1)\Big\} - \frac{\xi_2^2}{2\omega_K}\exp(i\frac{2\pi}{3}), \\
Q_2 &= \zeta_1 \exp[i\mathbf{k}\cdot(\mathbf{a}_2-\mathbf{a}_1)], \\
Q_3 &= -\frac{\xi_1\xi_2}{2\omega_K}\exp(-i\frac{2\pi}{3})\Big\{\exp[i\mathbf{k}\cdot(\mathbf{a}_2-\mathbf{a}_1)] + \exp(i\mathbf{k}\cdot\mathbf{a}_2)\Big\} - \frac{\xi_2^2}{2\omega_K}\exp(-i\frac{2\pi}{3}), \\
Q_4 &= -\frac{\xi_1\xi_2}{2\omega_K}\exp(i\frac{2\pi}{3})\Big\{\exp[i\mathbf{k}\cdot(\mathbf{a}_2-\mathbf{a}_1)] + \exp(i\mathbf{k}\cdot\mathbf{a}_2)\Big\} - \frac{\xi_2^2}{2\omega_K}\exp(i\frac{2\pi}{3}), \\
Q_5 &= -\frac{\xi_1\xi_2}{2\omega_K}\exp(-i\frac{2\pi}{3})[\exp(i\mathbf{k}\cdot\mathbf{a}_2) + \exp(i\mathbf{k}\cdot\mathbf{a}_1)] - \frac{\xi_2^2}{2\omega_K}\exp(-i\frac{2\pi}{3}), \\
Q_6 &= -\frac{\xi_1\xi_2}{2\omega_K}\exp(i\frac{2\pi}{3})[\exp(i\mathbf{k}\cdot\mathbf{a}_2) + \exp(i\mathbf{k}\cdot\mathbf{a}_1)] - \frac{\xi_2^2}{2\omega_K}\exp(i\frac{2\pi}{3}), \\
Q_7 &= -\frac{\xi_1\xi_2}{2\omega_K}\exp(i\frac{2\pi}{3})\Big\{\exp[i\mathbf{k}\cdot(\mathbf{a}_1-\mathbf{a}_2)] + \exp(i\mathbf{k}\cdot\mathbf{a}_1)\Big\} - \frac{\xi_2^2}{2\omega_K}\exp(i\frac{2\pi}{3}).
\end{aligned}
\tag{15.13}
$$

Topological invariants can be used to distinguish different phases. For any insulator with translational symmetry, the gauge-invariant Chern number of bulk bands [58, 138]

$$
C = \frac{i}{2\pi}\iint_{\mathrm{BZ}} dk_x dk_y \mathrm{Tr}\Big[P(\frac{\partial P}{\partial k_x}\frac{\partial P}{\partial k_y} - \frac{\partial P}{\partial k_y}\frac{\partial P}{\partial k_x})\Big] \tag{15.14}
$$

is often adopted for determining the FOTI phase, where P is projection matrix $P(\mathbf{k}) = \phi(\mathbf{k})\phi(\mathbf{k})^\dagger$, with $\phi(\mathbf{k})$ being the normalized eigenstate (column vector) of Hamiltonian, and the integral is over the first Brillouin zone. However, to determine whether the system allows the HOTI phase, another different topological invariant should be considered.

In the presence of six-fold rotational (C_6) symmetry, a proper topological invariant is the $\mathbb{Z}_6$ Berry phase [48–52]:

$$
\theta = \int_{L_1} \mathrm{Tr}[\mathbf{A}(\mathbf{k})]\cdot \mathrm{d}\mathbf{k} \pmod{2\pi}, \tag{15.15}
$$

where $\mathbf{A}(\mathbf{k})$ is the Berry connection:

$$
\mathbf{A}(\mathbf{k}) = i\Psi^\dagger(\mathbf{k})\frac{\partial}{\partial \mathbf{k}}\Psi(\mathbf{k}). \tag{15.16}
$$

Here, $\Psi(\mathbf{k}) = [\phi_1(\mathbf{k}),\phi_2(\mathbf{k}),\phi_3(\mathbf{k})]$ is the 6×3 matrix composed of the eigenvectors of (15.12) for the lowest three bands. L_1 is an integral path in momentum space $G' \to \Gamma \to K'$; see the green line segment in Fig. 15.19a. The Wilson-loop approach is adopted for evaluating the Berry phase θ to avoid the difficulty of the gauge choice [23, 24]. It is worth mentioning that the six high-symmetry points G, K, G', K', G'',

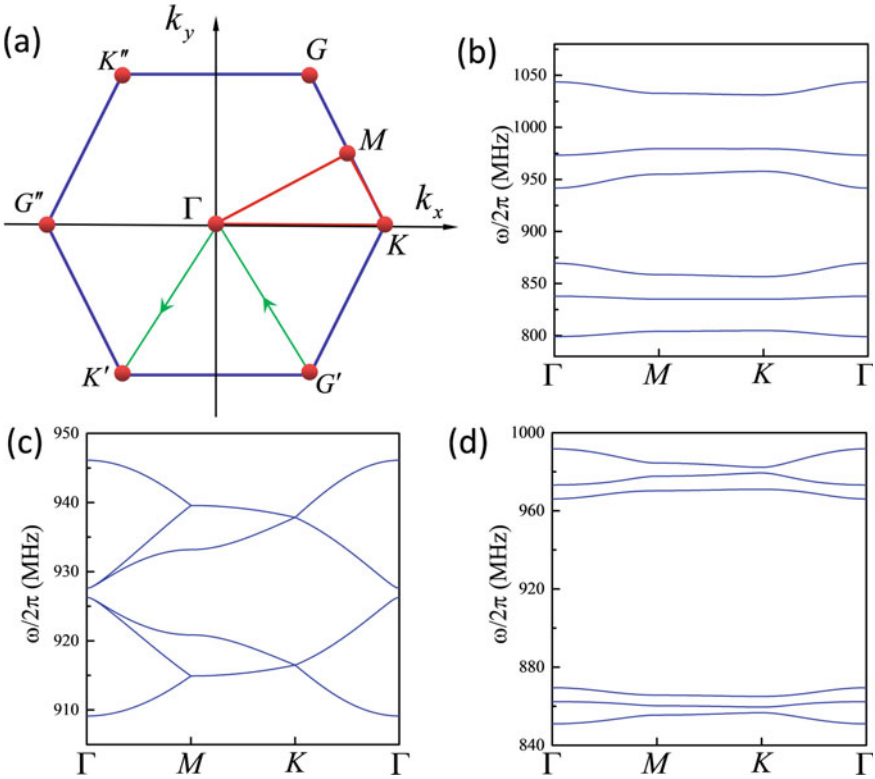

Fig. 15.19 **a** The first Brillouin zone of the breathing honeycomb lattice, with high-symmetry points Γ, G, M, and K located at $(k_x, k_y) = (0, 0)$, $(\frac{2\pi}{3a}, \frac{2\sqrt{3}\pi}{3a})$, $(\frac{\pi}{a}, \frac{\sqrt{3}\pi}{3a})$, and $(\frac{4\pi}{3a}, 0)$, respectively. Band structures along the loop Γ-M-K-Γ for different lattice parameters: $d_1 = 3.6r$, $d_2 = 2.08r$ (**b**), $d_1 = d_2 = 3.6r$ (**c**), and $d_1 = 2.08r$, $d_2 = 3.6r$ (**d**). Images are taken from [137]

and K'' in the first Brillouin zone are equivalent (see Fig. 15.19a), because of the C_6 symmetry. Therefore, there are other five equivalent integral paths ($L_2 : K' \to \Gamma \to G''$, $L_3 : G'' \to \Gamma \to K''$, $L_4 : K'' \to \Gamma \to G$, $L_5 : G \to \Gamma \to K$, and $L_6 : K \to \Gamma \to G'$) leading to the identical θ. It is also straightforward to see that the integral along the path $L_1 + L_2 + L_3 + L_4 + L_5 + L_6$ vanishes. Thus, the $\mathbb{Z}_6$ Berry phase must be quantized as $\theta = \frac{2n\pi}{6}$ $(n = 0, 1, 2, 3, 4, 5)$. By simultaneously quantifying the Chern number C and the $\mathbb{Z}_6$ Berry phase θ, the topological phases and their transition can be determined accurately.

Corner states are of particular interest and are deeply related to the symmetry of Hamiltonian (15.12). Below, we prove that the emergence of topological zero modes is protected by the generalized chiral symmetry. First of all, because $(\xi_1^2 + 2\xi_2^2)/2\omega_K \ll \omega_0$, the diagonal element of $\mathcal{H}$ can be regarded as a constant independent of d, i.e., $Q_0 = \omega_0$, which is the "zero-energy" of the original Hamiltonian. $Q_{1,2,3,4,5,6}$ are the next-nearest hopping terms. At first glance, the system

does not possess any chiral symmetry to protect the "zero-energy" modes because the breathing honeycomb lattice is not a bipartite lattice. Inspired by the explanation of generalized chiral symmetry in the breathing kagome lattice [37, 139], the chiral symmetry for a unit cell containing six sites can be generalized by defining

$$\begin{aligned}
\Gamma_6^{-1}\mathcal{H}_1\Gamma_6 &= \mathcal{H}_2,\\
\Gamma_6^{-1}\mathcal{H}_2\Gamma_6 &= \mathcal{H}_3,\\
\Gamma_6^{-1}\mathcal{H}_3\Gamma_6 &= \mathcal{H}_4,\\
\Gamma_6^{-1}\mathcal{H}_4\Gamma_6 &= \mathcal{H}_5,\\
\Gamma_6^{-1}\mathcal{H}_5\Gamma_6 &= \mathcal{H}_6,\\
\mathcal{H}_1+\mathcal{H}_2+\mathcal{H}_3+\mathcal{H}_4+\mathcal{H}_5+\mathcal{H}_6 &= 0,
\end{aligned} \tag{15.17}$$

where the chiral operator Γ_6 is a diagonal matrix to be determined, and $\mathcal{H}_1 = \mathcal{H} - Q_0\mathrm{I}$. Here, to prove the system has generalized chiral symmetry, we divide the system into six subgroups with the components of matrix Hamiltonian being nonzero only between different subgroups, such a property is essential for chiral symmetry and indicates no interaction within sublattices. Therefore, the matrices (H_2, H_3, etc.) are the subgroups used for explaining the chiral symmetry of system. Upon combining the last equation with the previous five in (15.17), we have $\Gamma_6^{-1}\mathcal{H}_6\Gamma_6 = \mathcal{H}_1$, implying that $[\mathcal{H}_1, \Gamma_6^6] = 0$; thus, $\Gamma_6^6 = \mathrm{I}$, via the reasoning completely analogous to the Su-Schrieffer-Heeger model [140]. Hamiltonians $\mathcal{H}_{1,2,3,4,5,6}$ each have the same set of eigenvalues $\lambda_{1,2,3,4,5,6}$. The eigenvalues of Γ_6 are given by $1,\ \exp(2\pi i/6),\ \exp(4\pi i/6),\ \exp(\pi i),\ \exp(8\pi i/6)$, and $\exp(10\pi i/6)$. Therefore, the matrix Γ_6 can written as

$$\Gamma_6 = \begin{pmatrix} 1 & 0 & 0 & 0 & 0 & 0\\ 0 & e^{\frac{2\pi i}{6}} & 0 & 0 & 0 & 0\\ 0 & 0 & e^{\frac{4\pi i}{6}} & 0 & 0 & 0\\ 0 & 0 & 0 & e^{\pi i} & 0 & 0\\ 0 & 0 & 0 & 0 & e^{\frac{8\pi i}{6}} & 0\\ 0 & 0 & 0 & 0 & 0 & e^{\frac{10\pi i}{6}} \end{pmatrix}, \tag{15.18}$$

in the same bases as expressing the Hamiltonian (15.12). By taking the trace of the sixth line from (15.17), we find $\sum_{i=1}^{6}\mathrm{Tr}(\mathcal{H}_i) = 6\mathrm{Tr}(\mathcal{H}_1) = 0$, which means that the sum of the six eigenvalues vanishes $\sum_{i=1}^{6}\lambda_i = 0$. Given an eigenstate ϕ_j that has support in only sublattice j, it will satisfy $\mathcal{H}_1\phi_j = \lambda\phi_j$ and $\Gamma_6\phi_j = \exp[2\pi i(j-1)/6]\phi_j$ with $j = 1, 2, 3, 4, 5, 6$. From these formulas and (15.17), one can find that $\sum_{i=1}^{6}\mathcal{H}_i\phi_j = \sum_{i=1}^{6}\Gamma_6^{-(i-1)}\mathcal{H}_1\Gamma_6^{i-1}\phi_j = 6\lambda\phi_j = 0$, indicating $\lambda = 0$ for any mode that has support in only one sublattice, i.e., zero-energy corner state.

15.5.2 Corner States and Phase Diagram

Figure 15.19b–d shows the bulk band structures under a variety of lattice parameters. For $d_1 = d_2 = 3.6r$ (see Fig. 15.19c), it can be found that the highest three bands and the lowest three bands merged separately, leaving a next-nearest hopping-induced gap centered at 927 MHz. In this case, the FOTI phase was anticipated [83, 125]. However, the six bands are separated from each other when considering the other two kinds of parameters (see Fig. 15.19b, d), indicating that the system is in the insulating state. These insulating phases and the phase transition point can be further distinguished by calculating Chern number and $\mathbb{Z}_6$ Berry phase.

Figure 15.20a plots the dependence of the Chern number (C) and the $\mathbb{Z}_6$ Berry phase (θ) on the parameter d_2/d_1. Here the material parameters of Py ($Ni_{80}Fe_{20}$) [88, 130] are used and fix $d_1 = 2.5r$. In addition, the eigenfrequencies of collective vortex gyration under different ratios d_2/d_1 for a parallelogram-shaped (see Fig. 15.20b) structure are also shown in Fig. 15.20c. By considering the topological invariants and spectrum simultaneously, one can infer that the system is in the trivial phase when $d_2/d_1 < 0.9$ and $1.08 < d_2/d_1 < 1.49$, in the FOTI phase when $0.9 < d_2/d_1 < 1.08$, and in the HOTI phase when $d_2/d_1 > 1.49$. Haldane model is a well-known example for breaking the time-reversal symmetry [134]. If we consider the limit case of honeycomb lattice, i.e., $d_1 = d_2$, (15.9) can be exactly mapped to the Haldane model, as shown in [83] and [125]. The very existence of the chiral edge state is thus naturally expected. For a breathing honeycomb lattice, our (15.11) represents the generalized form of the mapping, where the last two terms in the right-hand side are the next-to-nearest hopping that breaks the time-reversal symmetry. The complete phase diagram of system can be obtained by systematically changing d_1 and d_2, with the results plotted in Fig. 15.20d: The regions labeled gray, white, and red represent the trivial, FOTI, and HOTI phases, respectively. Importantly, we find that the boundary for the phase transition between trivial and FOTI phases depends only weakly on the choice of the absolute values of d_1 and d_2 but is (almost) solely determined by their ratio, as indicated by dashed black lines ($l_1 : d_2/d_1 = 0.94$ and $l_2 : d_2/d_1 = 1.05$) in the figure. However, the boundary for the phase transition between trivial and HOTI phases is a linear function $l_3 : d_2 = 2.24d_1 - 1.88$ (see the dashed red line in Fig. 15.20d). It is worth noting that the topological charge of the vortex has no influence on higher-order topology for the reason that the sign of topological charge just determines the direction (clockwise or anti-clockwise) of gyration, see (15.5). However, it indeed can affect the chiral edge state (first-order topology). Namely the chirality of edge state will be reversed if the topological charge changes.

The existence of symmetry-protected states on boundaries is the hallmark of a topological insulating phase. Figure 15.21b–d shows the energy spectrum of the ribbon configuration with armchair edges (see Fig. 15.21a) for different choices of d_1 and d_2. For $d_1 = 3.6r$ and $d_2 = 2.08r$ (black star in Fig. 15.20d), the system is in the trivial phase without any topological edge mode (see Fig. 15.21b). For $d_1 = d_2 = 3.6r$ (blue star in Fig. 15.20d), the lattice considered is identical to a magnetic texture version of graphene (the perfect honeycomb lattice). In contrast to

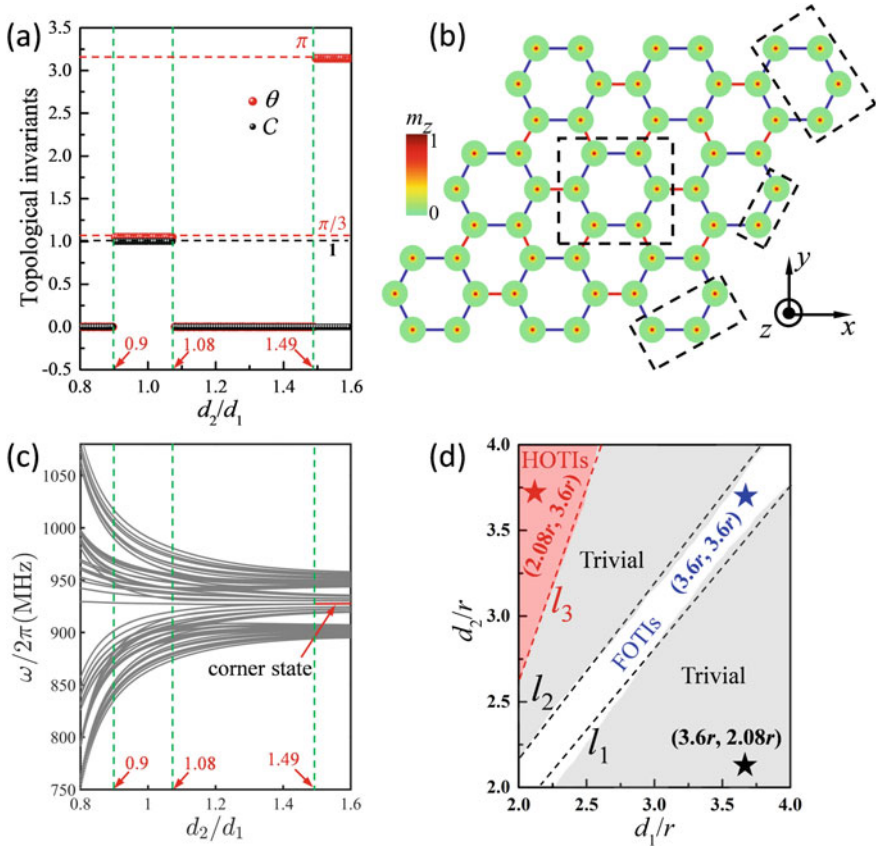

Fig. 15.20 **a** Dependence of the topological invariants Chern number and $\mathbb{Z}_6$ Berry phase on the ratio d_2/d_1 when d_1 is fixed at $2.5r$. **b** Schematic plot of the parallelogram-shaped vortex lattice with armchair edges. **c** Eigenfrequencies of collective vortex gyration under different ratios d_2/d_1 with the red segment denoting the corner state phase. **d** Phase diagram of the system with pentagonal stars of different colors representing three typical parameters of d_1 and d_2 for different phases considered in the subsequent calculations and analyses. Images are taken from [137]

the gapless band structure for perfect graphene nanoribbons, the imaginary second-nearest hopping term opens a gap at the Dirac point and supports a topologically protected first-order chiral edge state [83, 125]. For $d_1 = 2.08r$ and $d_2 = 3.6r$ (red star in Fig. 15.20d), one can clearly see two distinct edge bands, in addition to bulk ones, as shown in Fig. 15.21d. These localized modes are actually not topological because they maintain the bidirectional propagation nature, which is justified by the fact that the wave group-velocity $d\omega/dk_x$ can be either positive or negative at different k_x points. Below, we will show that higher-order topological corner states exactly emerge around these edge bands when the system is decreased to be finite in both dimensions.

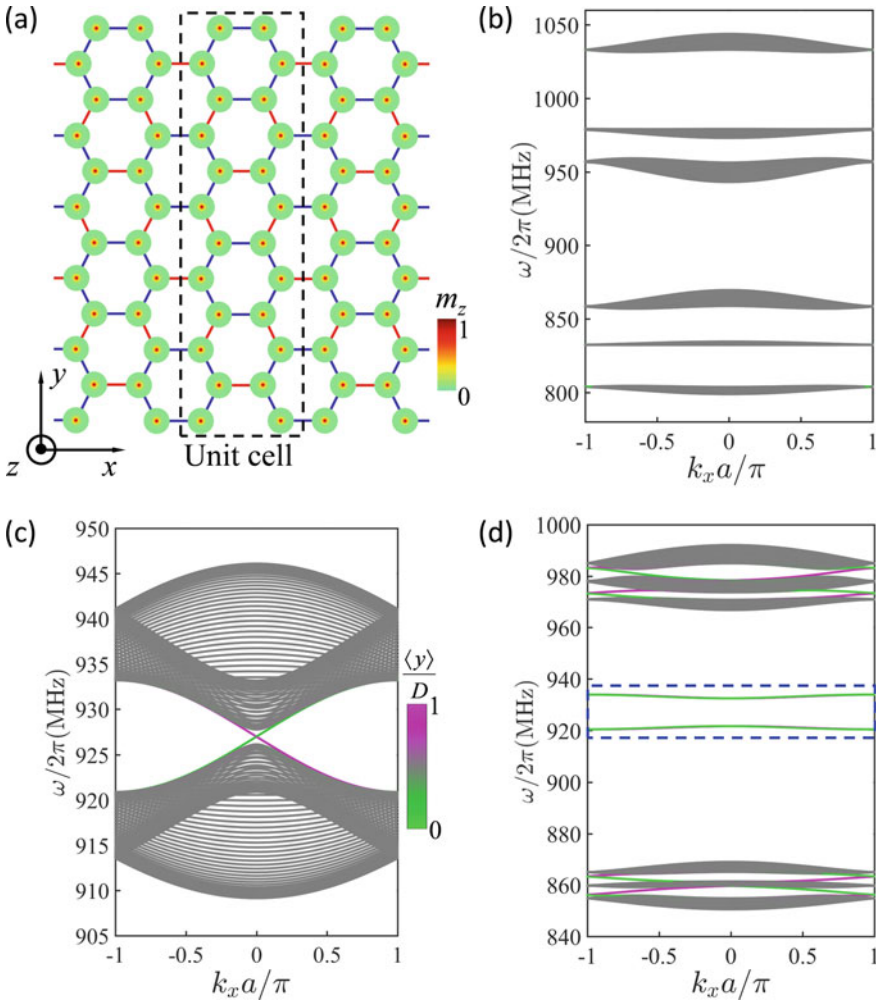

Fig. 15.21 **a** Nanoribbon with armchair edges (closed boundaries in the x-direction and open boundaries in the y-direction). The dashed black rectangle is the unit cell. Band dispersions with different geometric parameters as denoted in Fig. 15.20d: $d_1 = 3.6r$, $d_2 = 2.08r$ (**b**), $d_1 = d_2 = 3.6r$ (**c**), and $d_1 = 2.08r$, $d_2 = 3.6r$ (**d**). The dashed blue frame in (**d**) indicates the band of non-chiral edge states. D is the width of the nanoribbon. Images are taken from [137]

A parallelogram-shaped vortex lattice is considered to visualize the second-order corner states, as shown in Fig. 15.20b, where $d_1 = 2.08r$ and $d_2 = 3.6r$. From the spectrum (see Fig. 15.22a), one can clearly see that there exist a few degenerate modes in the band gap. To distinguish these states, the spatial distribution of vortex gyrations are plotted for each mode in Fig. 15.22b–f. Three types of corner states are confirmed, all of which have oscillations highly localized at obtuse-angled or

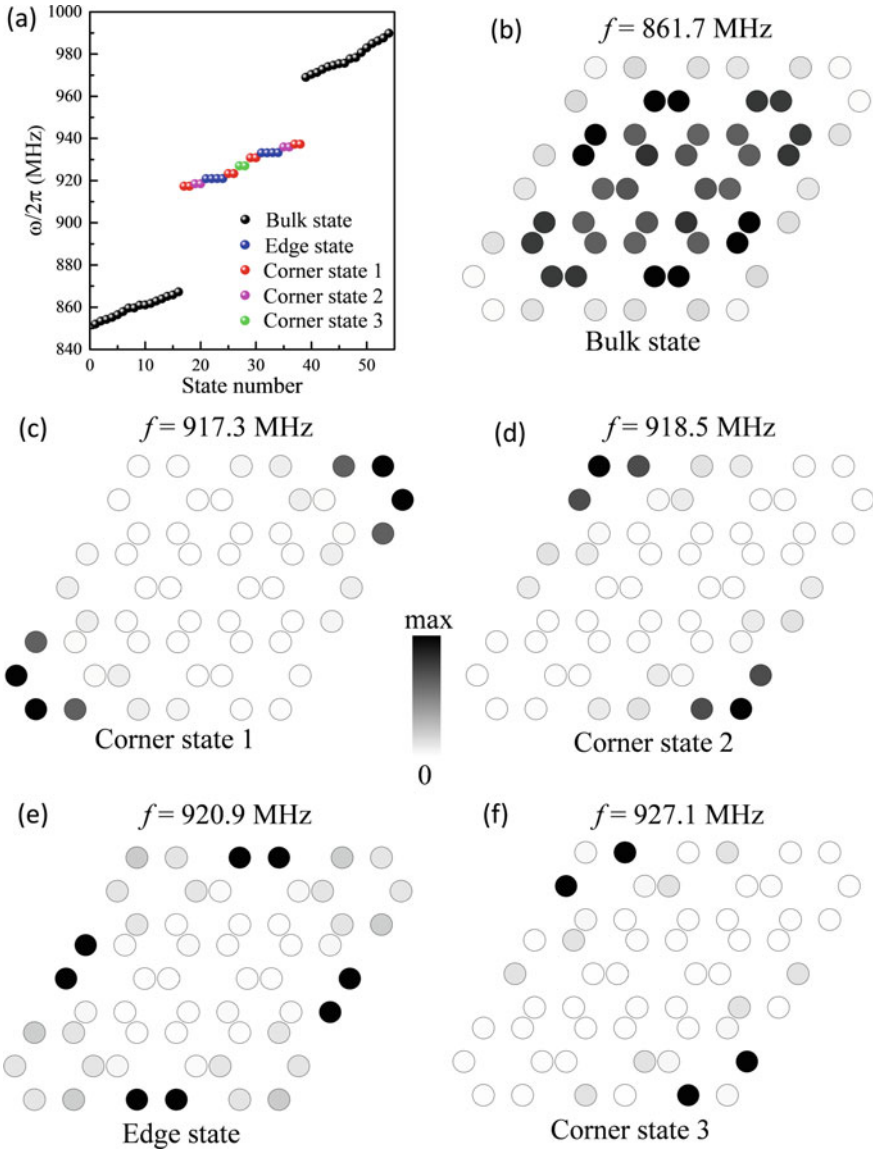

Fig. 15.22 **a** Eigenfrequencies of the finite system with parameters $d_1 = 2.08r$ and $d_2 = 3.6r$ for the parallelogram-shaped structure (see Fig. 15.3b). The spatial distribution of vortex gyrations for the bulk (**b**), corner (**c**, **d** and **f**), and edge (**e**) states of five representative frequencies. Images are taken from [137]

acute-angled corners (see Fig. 15.22c, d, f), where corner states 1 (type I), 2 (type II), and 3 (type III) are denoted by red, magenta, and green balls, respectively. Two degenerate edge modes are denoted by blue balls, in which only two vortices on each

edge participate in the oscillation, as shown in Fig. 15.22e. Figure 15.22b shows the bulk state with oscillations spreading over the whole lattice except the boundaries. To judge whether these edge and corner states are topologically protected or not, moderate defects and disorder are introduced into the system and we evaluate the change of the spectrum. It can be found that the eigenfrequency of "zero-energy" corner state 3 at the obtuse-angled corner (see Fig. 15.22f) is well confined around 927 MHz, which means that this corner state is suitably immune from external frustrations. This feature is due to the topological protection from the generalized chiral symmetry. However, the frequencies of other corner modes (Fig. 15.22c, d) have obvious shifts, revealing that these crystalline-symmetry-induced modes are sensitive to disorder. The origin of the edge state (Fig. 15.22e) is again attributed to the so-called Tamm-Shockley mechanism [118, 119].

To figure out why the chiral symmetry-protected (CSP) corner modes emerge at only obtuse-angled corners instead of acute-angled corners, the topological index $\mathcal{N} = |\mathcal{N}_+ - \mathcal{N}_-|$ is introduced, which captures the interplay between the topology of the bulk Hamiltonian and the defect structure [31, 141]. Here, $\mathcal{N}$ counts the number of topologically stable modes bound to corners, and $\mathcal{N}_\pm$ are integers counting the number of eigenstates of the chiral symmetry operator $\hat{\Pi}$ with eigenvalues $+1$ and -1, respectively. In the zero-correlation length limit $d_2 \to \infty$, the breathing honeycomb lattice is then reduced to isolated dimers (see Fig. 15.23b). As long as the gap is not closed, the symmetry and the Berry phase remain, as evidenced by the topological invariant θ. When the system is in the HOTI phase, $\mathcal{N}_+ = \mathcal{N}_- = 1$ in each edge unit cell and $\mathcal{N}_+ = \mathcal{N}_- = 2$ for acute-angled corners, such that $\mathcal{N} = 0$, indicating that there may exist non-CSP modes at acute-angled corners or edges. However, a similar analysis results in totally different outcome for obtuse-angled corners: $\mathcal{N}_+ = 1$ and $\mathcal{N}_- = 2$ or $\mathcal{N}_+ = 2$ and $\mathcal{N}_- = 1$, which leads to $\mathcal{N} = 1$. Thus, CSP or "zero-energy" modes must exist in each obtuse-angled corner. It is worth noting that the "zero-energy" corner state appears at acute-angled corners rather than obtuse-angled corners if the edges of lattice change to zigzag type. This result also can be fully explained in terms of the topological index $\mathcal{N}$ (see Fig. 15.23d, e).

On the other hand, in the limit $d_1 \to \infty$ (see Fig. 15.23c, f), we find that there are no uncoupled vortices. The six corners of the isolated hexagon are equivalent, with no special edge or corner states.

15.5.3 Micromagnetic Simulations

The micromagnetic simulations are implemented to verify theoretical predictions. Here, the parallelogram-shaped breathing honeycomb lattice of magnetic vortices with an armchair edge is considered, as shown in Fig. 15.20b. All material parameters are the same as those for theoretical calculations in Fig. 15.21d. The numerical package MUMAX3 [117] is used to simulate the collective dynamics of vortex lattice.

Figure 15.24a shows the temporal Fourier spectra of the vortex oscillations at different positions, with the black, red, blue, and green curves indicating the positions

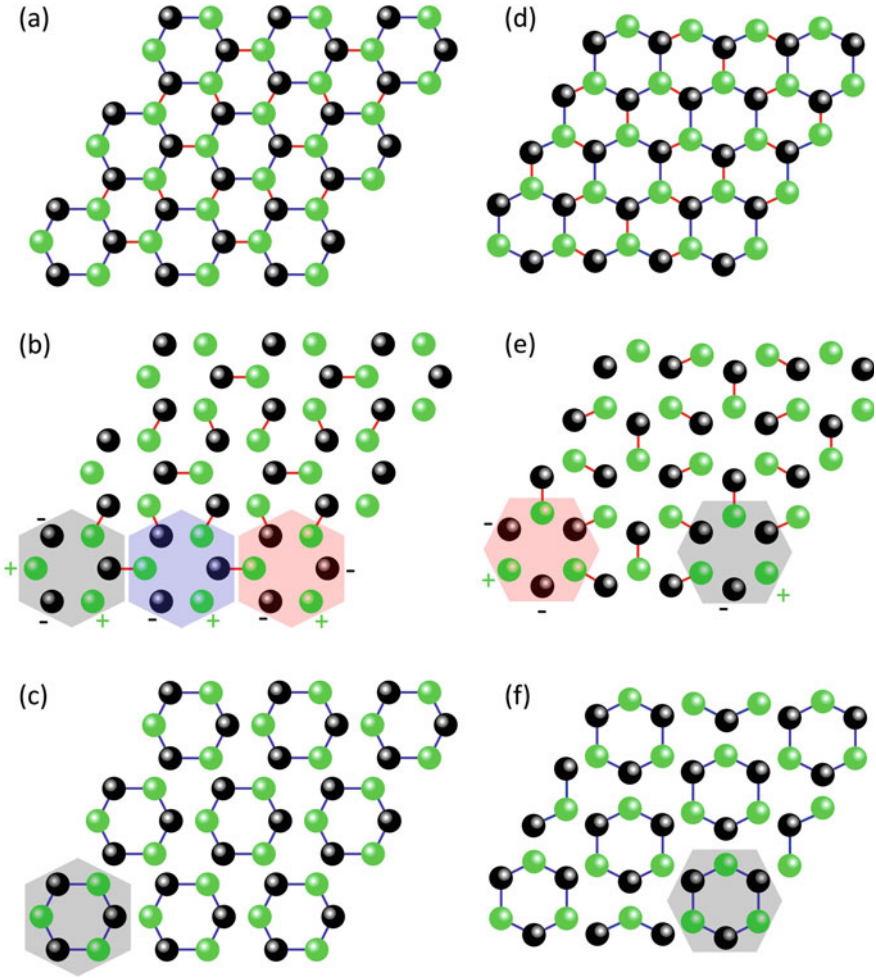

Fig. 15.23 The configuration of breathing honeycomb lattices of magnetic vortices with armchair (**a**) and zigzag edges (**d**). (**b**) and (**e**) [(**c**) and (**f**)] are the corresponding configurations of (**a**) and (**d**) in the zero-correlation length limit $d_2 \to \infty$ ($d_1 \to \infty$), respectively, which consist of isolated dimers (hexamer). Green and black balls indicate eigenvalues of $+1$ and -1 of the chiral-symmetry operator, respectively. Shaded areas represent the unit cell at different positions. Images are taken from [137]

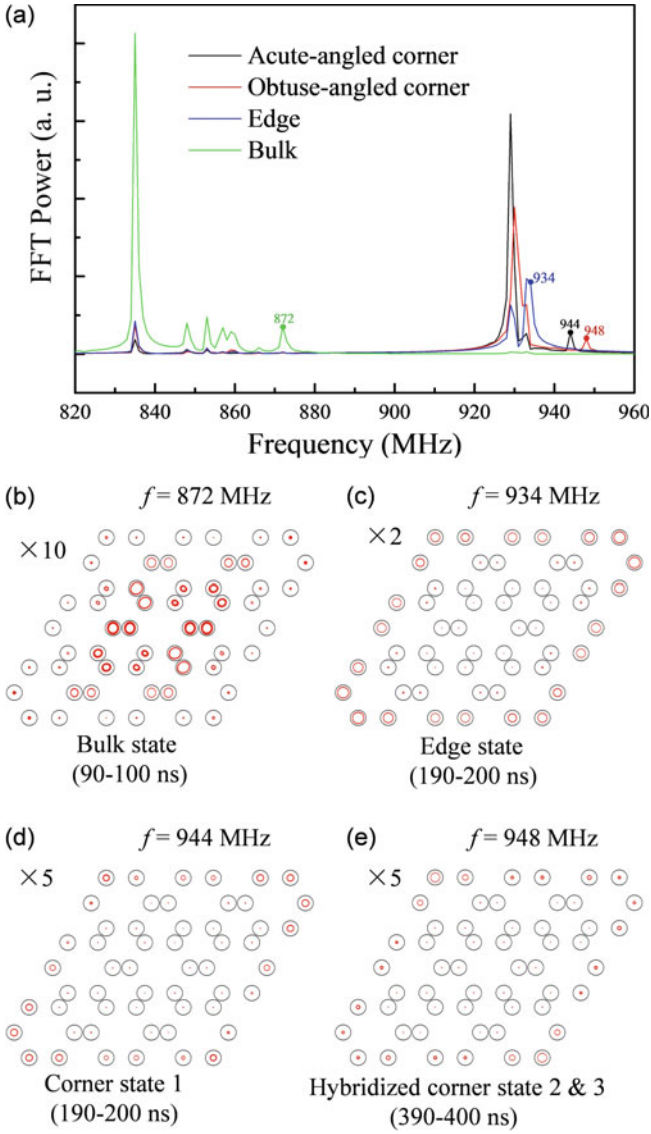

Fig. 15.24 **a** The temporal Fourier spectra of the vortex oscillations at different positions marked by dashed black rectangles in Fig. 15.20b. The gyration path for all vortices under excitation fields with different frequencies, 872 MHz (**b**), 934 MHz (**c**), 944 MHz (**d**), and 948 MHz (**e**). Since the oscillation amplitudes of the vortex centers are too small, we have magnified them by 2, 5 or 10 times, as labeled in each figure. Images are taken from [137]

of acute-angled corner, obtuse-angled corner, edge, and bulk bands, respectively. It can be seen that around the frequency of 944 MHz (948 MHz), the spectra for acute-angled corner (obtuse-angled corner) have an obvious peak, which does not happen for the spectra for edge and bulk bands. Therefore, these two peaks denote two different corner states that are located at acute-angled or obtuse-angled corners. Similarly, the frequency range for bulk and edge states is identified. Further, to visualize the spatial distribution of the vortex oscillations for different modes, four representative frequencies are chosen and are marked by green, blue, black, and red dots: 872 MHz for the bulk state, 934 MHz for the edge state, 944 MHz for the acute-angled corner state, and 948 MHz for the obtuse-angled corner state, respectively. We then stimulate their dynamics by applying a sinusoidal field to the whole system. The 10 ns gyration paths of all vortices are plotted in Fig. 15.24b–e when the excitation field drives a steady-state vortex dynamics. The spatial distribution of vortices motion for the bulk and edge states are shown in Fig. 15.24b, c, respectively. We observe type I corner state with vortex oscillation localized at the acute-angled corner in Fig. 15.24d, which is in good agreement with the theoretical result. Interestingly, we note a strong hybridization between the type II and type III corner states, as shown in Fig. 15.22f, which is because their frequencies are very close to each other and their wavefunctions have a large overlap (see Fig. 15.22).

15.6 Conclusion and Outlook

We have introduced the concept of topological insulator (both first-order and higher-order) based on spin texture metamaterials. The emerging multiband chiral edge modes possessing different handness in skyrmion lattice should be appealing for designing future skyrmionic topological devices. Besides, the predicted second-order insulating phase in vortex lattice can facilitate designing new functional devices based on magnetic solitons. For instance, we can realize a magnetic imaging system by designing one vortex lattice of the desired shape in the HOTI phase surrounded by another vortex lattice in the trivial phase [142, 143]. It is noted that the unique localization property of vortex gyrations strongly depends on the working frequency, which would motivate us to devise magnetic nano-oscillators with high spatiotemporal resolution. Furthermore, the multiband nature of corner modes (spectrum ranging from sub GHz to dozens of GHz) is very useful to design broad-band topological devices. In the present model, we have considered nanodisks with identical radius. When the translational symmetry is broken, for instance, by introducing Kekulé distortions to disk sizes, one may realize novel devices supporting robust Majorana-like zero modes localized in the device's geometric center [144]. From an experimental point of view, the fabrication of artificial vortex or skyrmion lattices is readily within reach of current technology, e.g., electron-beam lithography [78, 79, 145] or X-ray illumination [146]. By tracking the nanometer-scale vortex orbits using the recently developed ultrafast Lorentz microscopy technique in a time-resolved manner [147], one can directly observe the second-order topological corner states.

Acknowledgements This work was supported by the National Natural Science Foundation of China (NSFC) (Grants No. 12074057, 11604041 and 11704060), the National Key Research Development Program under Contract No. 2016YFA0300801, and the National Thousand-Young-Talent Program of China. Z.-X. L. acknowledges the financial support of NSFC under Grant No. 11904048 and the China Postdoctoral Science Foundation under Grant No. 2019M663461. We acknowledged Z.Y.W, C.W. and X.S.W. for helpful discussions.

References

1. M.Z. Hasan, C.L. Kane, Rev. Mod. Phys. **82**, 3045 (2010)
2. X.-L. Qi, S.-C. Zhang, Rev. Mod. Phys. **83**, 1057 (2011)
3. J.E. Moore, Nature **464**, 194–198 (2010)
4. C.L. Kane, E.J. Mele, Phys. Rev. Lett. **95**, 226801 (2005)
5. C.L. Kane, E.J. Mele, Phys. Rev. Lett. **95**, 146802 (2005)
6. L. Lu, J.D. Joannopoulos, M. Soljacic, Nat. Photon. **8**, 821–829 (2014)
7. A.B. Khanikaev, G. Shvets, Nat. Photon. **11**, 763–773 (2017)
8. G. Harari, M. A. Bandres, Y. Lumer et al., Science **359**, eaar4003 (2018)
9. M. A. Bandres, S. Wittek, G. Harari et al., Science **359**, eaar4005 (2018)
10. T. Ozawa, H.M. Price, A. Amo et al., Rev. Mod. Phys. **91**, 015006 (2019)
11. J. Paulose, B.G.G. Chen, V. Vitelli, Nat. Phys. **11**, 153–156 (2015)
12. L.M. Nash, D. Kleckner, A. Read et al., PNAS **112**, 14495 (2015)
13. S.D. Huber, Nat. Phys. **12**, 621–623 (2016)
14. N.P. Mitchell, L.M. Nash, D. Hexner et al., Nat. Phys. **14**, 380–385 (2018)
15. Z. Yang, F. Gao, X. Shi et al., Phys. Rev. Lett. **114**, 114301 (2015)
16. C. He, X. Ni, H. Ge et al., Nat. Phys. **12**, 1124–1129 (2016)
17. R. Fleury, A.B. Khanikaev, A. Alù, Nat. Commun. **7**, 11744 (2016)
18. X. Zhang, M. Xiao, Y. Cheng et al., Commun. Phys. **1**, 97 (2018)
19. L. Zhang, J. Ren, J.-S. Wang et al., Phys. Rev. B **87**, 144101 (2013)
20. A. Mook, J. Henk, I. Mertig, Phys. Rev. B **90**, 024412 (2014)
21. R. Chisnell, J.S. Helton, D.E. Freedman et al., Phys. Rev. Lett. **115**, 147201 (2015)
22. A. Ruckriegel, A. Brataas, R.A. Duine, Phys. Rev. B **97**, 081106(R) (2018)
23. W.A. Benalcazar, B.A. Bernevig, T.L. Hughes, Science **357**, 61–66 (2017)
24. W.A. Benalcazar, B.A. Bernevig, T.L. Hughes, Phys. Rev. B **96**, 245115 (2017)
25. M. Ezawa, Phys. Rev. Lett. **120**, 026801 (2018)
26. Z. Song, Z. Fang, C. Fang, Phys. Rev. Lett. **119**, 246402 (2017)
27. J. Langbehn, Y. Peng, L. Trifunovic et al., Phys. Rev. Lett. **119**, 246401 (2017)
28. F. Schindler, A.M. Cook, M.G. Vergniory et al., Sci. Adv. **4**, eaat0346 (2018)
29. R. Queiro, A. Stern, Phys. Rev. Lett. **123**, 036802 (2019)
30. B.-Y. Xie, H.-F. Wang, H.-X. Wang et al., Phys. Rev. B **98**, 205147 (2018)
31. J. Noh, W.A. Benalcazar, S. Huang et al., Nat. Photon. **12**, 408–415 (2018)
32. A.E. Hassan, F.K. Kunst, A. Moritz et al., Nat. Photon. **13**, 697–700 (2019)
33. S. Mittal, V.V. Orre, G. Zhu et al., Nat. Photon. **13**, 692–696 (2019)
34. X.-D. Chen, W.-M. Deng, F.-L. Shi et al., Phys. Rev. Lett. **122**, 233902 (2019)
35. B.-Y, Xie, G.-X. Su, H.-F. Wang et al., Phys. Rev. Lett. **122**, 233903 (2019)
36. H. Xue, Y. Yang, F. Gao et al., Nat. Mater. **18**, 108–112 (2019)
37. X. Ni, M. Weiner, A. Alu et al., Nat. Mater. **18**, 113–120 (2019)
38. H. Xue, Y. Yang, G. Liu et al., Phys. Rev. Lett. **122**, 244301 (2019)
39. C. He, S.-Y. Yu, H. Wang et al., Phys. Rev. Lett. **123**, 195503 (2019)
40. X. Zhang, H.-X. Wang, Z.-K. Lin et al., Nat. Phys. **15**, 582–588 (2019)
41. S. Imhof, C. Berger, F. Bayer et al., Nat. Phys. **14**, 925–929 (2018)
42. M. Ezawa, Phys. Rev. B **98**, 201402(R) (2018)

43. M. Serra-Garcia, R. Süsstrunk, S.D. Huber, Phys. Rev. B **99**, 020304(R) (2019)
44. J. Bao, D. Zou, W. Zhang et al., Phys. Rev. B **100**, 201406(R) (2019)
45. H. Yang, Z.-X. Li, Y. Liu et al., Phys. Rev. Research **2**, 022028(R) (2020)
46. Y. Xu, R. Xue, S. Wan,. arXiv:1711.09202
47. R.-J. Slager, L. Rademaker, J. Zaanen et al., Phys. Rev. B **92**, 085126 (2015)
48. J. Zak, Phys. Rev. Lett. **62**, 2747 (1989)
49. T. Kariyado, T. Morimoto, Y. Hatsugai, Phys. Rev. Lett. **120**, 247202 (2018)
50. Y. Hatsugai, I. Maruyama, Europhys. Lett. **95**, 20003 (2011)
51. H. Wakao, T. Yoshida, H. Araki et al., Phys. Rev. B **101**, 094107 (2020)
52. H. Araki, T. Mizoguchi, Y. Hatsugai, Phys. Rev. Res. **2**, 012009(R) (2020)
53. A.V. Chumak, V.I. Vasyuchka, A.A. Serga et al., Nat. Phys. **11**, 453–461 (2015)
54. V.V. Kruglyak, S.O. Demokritov, D. Grundler, J. Phys. D **43**, 264001 (2010)
55. R. Shindou, J.-I. Ohe, R. Matsumoto et al., Phys. Rev. B **87**, 174402 (2013)
56. A.L. Chernyshev, P.A. Maksimov, Phys. Rev. Lett. **117**, 187203 (2016)
57. S.K. Kim, H. Ochoa, R. Zarzuela et al., Phys. Rev. Lett. **117**, 227201 (2016)
58. X.S. Wang, Y. Su, X.R. Wang, Phys. Rev. B **95**, 014435 (2017)
59. X.S. Wang, H.W. Zhang, X.R. Wang, Phys. Rev. Appl. **9**, 024029 (2018)
60. L. Chen, J.-H. Chung, B. Gao et al., Phys. Rev. X **8**, 041028 (2018)
61. A. Wachowiak, J. Wiebe, M. Bode et al., Science **298**, 577–580 (2002)
62. B.V. Waeyenberge, A. Puzic, H. Stoll et al., Nature **444**, 461–464 (2006)
63. I. Makhfudz, B. Kruger, O. Tchernyshyov, Phys. Rev. Lett. **109**, 217201 (2012)
64. K.W. Moon, B.S. Chun, W. Kim et al., Phys. Rev. B **89**, 064413 (2014)
65. D. Petit, P.R. Seem, M. Tillette et al., Appl. Phys. Lett. **106**, 022402 (2015)
66. S. Mühlbauer, B. Binz, F. Jonietz et al., Science **323**, 915–919 (2009)
67. W. Jiang, P. Upadhyaya, W. Zhang et al., Science **349**, 283–286 (2015)
68. D.A. Allwood, G. Xiong, C.C. Faulkner et al., Science **309**, 1688–1692 (2005)
69. M. Hayashi, L. Thomas, R. Moriya et al., Science **320**, 209–211 (2008)
70. G. Catalan, J. Seidel, R. Ramesh et al., Rev. Mod. Phys. **84**, 119 (2012)
71. S.S.P. Parkin, M. Hayashi, L. Thomas, Science **320**, 190–194 (2008)
72. S. Parkin, S.-H. Yang, Nat. Nanotech. **10**, 195–198 (2015)
73. F. Jonietz, S. Mühlbauer, C. Pfleiderer et al., Science **330**, 1648–1651 (2010)
74. X.Z. Yu, N. Kanazawa, W.Z. Zhang et al., Nat. Commun. **3**, 988 (2012)
75. V.S. Pribiag, I.N. Krivorotov, G.D. Fuchs et al., Nat. Phys. **3**, 498–503 (2007)
76. G. Hrkac, P.S. Keatley, M.T. Bryan et al., J. Phys. D **48**, 453001 (2015)
77. S. Zhang, J. Wang, Q. Zheng et al., New J. Phys. **17**, 023061 (2015)
78. D.S. Han, A. Vogel, H. Jung et al., Sci. Rep. **3**, 2262 (2013)
79. C. Behncke, M. Hänze, C.F. Adolff et al., Phys. Rev. B **91**, 224417 (2015)
80. M. Hänze, C.F. Adolff, B. Schulte et al., Sci. Rep. **6**, 22402 (2016)
81. J. Kim, J. Yang, Y.-J. Cho et al., Sci. Rep. **7**, 45185 (2017)
82. M. Mruczkiewicz, P. Gruszecki, M. Zelent et al., Phys. Rev. B **93**, 174429 (2016)
83. S.K. Kim, Y. Tserkovnyak, Phys. Rev. Lett. **119**, 077204 (2017)
84. A. Vogel, A. Drews, T. Kamionka et al., Phys. Rev. Lett. **105**, 037201 (2010)
85. H. Jung, K.-S. Lee, D.-E. Jeong et al., Sci. Rep. **1**, 59 (2011)
86. S. Sugimoto, Y. Fukuma, S. Kasai et al., Phys. Rev. Lett. **106**, 197203 (2011)
87. M. Hänze, C.F. Adolff, S. Velten et al., Phys. Rev. B **93**, 054411 (2016)
88. S. Velten, R. Streubel, A. Farhan et al., Appl. Phys. Lett. **110**, 262406 (2017)
89. M.Y. Im, P. Fischer, H.-S. Han et al., NPG Asia Mater. **9**, e348 (2017)
90. A. Fert, V. Cros, J. Sampaio, Nat. Nanotech. **8**, 152–156 (2013)
91. A.A. Thiele, Phys. Rev. Lett. **30**, 230 (1973)
92. F. Büttner, C. Moutafis, M. Schneider et al., Nat. Phys. **11**, 225–228 (2015)
93. X.Z. Yu, Y. Onose, N. Kanazawa et al., Nature **465**, 901–904 (2010)
94. N. Romming, C. Hanneken, M. Menzel et al., Science **341**, 636–639 (2013)
95. X. Zhang, M. Ezawa, D. Xiao et al., Nanotechnology **26**, 225701 (2015)
96. C. Psaroudaki, D. Loss, Phys. Rev. Lett. **120**, 237203 (2018)

97. W. Wang, M. Beg, B. Zhang et al., Phys. Rev. B **92**, 020403(R) (2015)
98. B. Zhang, W. Wang, M. Beg et al., Appl. Phys. Lett. **106**, 102401 (2015)
99. K. Everschor, M. Garst, B. Binz et al., Phys. Rev. B **86**, 054432 (2012)
100. L. Kong, J. Zang, Phys. Rev. Lett. **111**, 067203 (2013)
101. S.-Z. Lin, C.D. Batista, C. Reichhardt et al., Phys. Rev. Lett. **112**, 187203 (2014)
102. W. Yang, H. Yang, Y. Cao et al., Opt. Express **26**, 8778 (2018)
103. Y. Jiang, H.Y. Yuan, Z.-X. Li et al., Phys. Rev. Lett. **124**, 217204 (2020)
104. K. Litzius, I. Lemesh, B. Krüger et al., Nat. Phys. **13**, 170–175 (2017)
105. W. Jiang, X. Zhang, G. Yu et al., Nat. Phys. **13**, 162–169 (2017)
106. X. Zhang, Y. Zhou, M. Ezawa, Nat. Commun. **7**, 10293 (2016)
107. X. Zhang, Y. Zhou, M. Ezawa, Sci. Rep. **6**, 24795 (2016)
108. J. Barker, O.A. Tretiakov, Phys. Rev. Lett. **116**, 147203 (2016)
109. H. Yang, C. Wang, T. Yu et al., Phys. Rev. Lett. **121**, 197201 (2018)
110. X. Wang, X.S. Wang, C. Wang et al., J. Phys. D **52**, 225001 (2019)
111. X. Zhang, M. Ezawa, Y. Zhou, Sci. Rep. **5**, 9400 (2015)
112. W. Kang, Y. Huang, C. Zheng et al., Sci. Rep. **6**, 23164 (2016)
113. S. Luo, M. Song, X. Li et al., Nano Lett. **18**, 1180–1184 (2018)
114. H. Yang, C. Wang, X. Wang et al., Phys. Rev. B **98**, 014433 (2018)
115. R. Tomasello, E. Martinez, R. Zivieri et al., Sci. Rep. **4**, 6784 (2014)
116. S. Seki, X.Z. Yu, S. Ishiwata et al., Science **336**, 198–201 (2012)
117. A. Vansteenkiste, J. Leliaert, M. Dvornik et al., AIP Adv. **4**, 107133 (2014)
118. I. Tamm, Phys. Z. Sowjetunion. **76**, 849 (1932)
119. W. Shockley, Phys. Rev. **56**, 317 (1939)
120. F.G. Mertens, H.J. Schnitzer, A.R. Bishop, Phys. Rev. B **56**, 2510 (1997)
121. B.A. Ivanov, G.G. Avanesyan, A.V. Khvalkovskiy et al., JETP Lett. **91**, 178 (2010)
122. S.S. Cherepov, B.C. Koop, A.Yu. Galkin et al., Phys. Rev. Lett. **109**, 097204 (2012)
123. J. Shibata, K. Shigeto, Y. Otani, Phys. Rev. B **67**, 224404 (2003)
124. J. Shibata, Y. Otani, Phys. Rev. B **70**, 012404 (2004)
125. Z.-X. Li, C. Wang, Y. Cao et al., Phys. Rev. B **98**, 180407(R) (2018)
126. Z.-X. Li, Y. Cao, P. Yan et al., npj Comput. Mater. **5**, 107 (2019)
127. K.S. Lee, H. Jung, D.S. Han et al., J. Appl. Phys. **110**, 113903 (2011)
128. O.V. Sukhostavets, J. González, K.Y. Guslienko, Phys. Rev. B **87**, 094402 (2013)
129. J.P. Sinnecker, H. Vigo-Cotrina, F. Garcia et al., J. Appl. Phys. **115**, 203902 (2014)
130. M.W. Yoo, J. Lee, S.K. Kim, Appl. Phys. Lett. **100**, 172413 (2012)
131. R.D. King-Smith, D. Vanderbilt, Phys. Rev. B **47**, 1651 (1993)
132. D. Vanderbilt, R.D. King-Smith, Phys. Rev. B **48**, 4442 (1993)
133. A.H. Castro Neto, F. Guinea, N.M.R. Peres et al., Rev. Mod. Phys. **81**, 109 (2009)
134. F.D.M. Haldane, Phys. Rev. Lett. **61**, 2015 (1988)
135. Y. Yao, F. Ye, X.-L. Qi et al., Phys. Rev. B **75**, 041401(R) (2007)
136. H. Fan, B. Xia, L. Tong et al., Phys. Rev. Lett. **122**, 204301 (2019)
137. Z.-X. Li, Y. Cao, X. R. Wang et al., Phys. Rev. Appl. **13**, 064058 (2020)
138. J.E. Avron, R. Seiler, B. Simon, Phys. Rev. Lett. **51**, 51 (1983)
139. S.N. Kempkes, M.R. Slot, J.J. van den Broeke et al., Nat. Mater. **18**, 1292–1297 (2019)
140. W.P. Su, J.R. Schrieffer, A.J. Heeger, Phys. Rev. Lett. **42**, 1698 (1979)
141. J.C.Y. Teo, C.L. Kane, Phys. Rev. B **82**, 115120 (2010)
142. Z. Zhang, H. Long, C. Liu et al., Adv. Mater. **31**, 1904682 (2019)
143. Z.-X. Li, Y. Cao, X.R. Wang et al., Phys. Rev. B **101**, 184404 (2020)
144. P. Gao, D. Torrent, F. Cervera et al., Phys. Rev. Lett. **123**, 196601 (2019)
145. L. Sun, R.X. Cao, B.F. Miao et al., Phys. Rev. Lett. **110**, 167201 (2013)
146. Y. Guang, I. Bykova, Y. Liu et al., Nat. Commun. **11**, 949 (2020)
147. M. Möller, J.H. Gaida, S. Schäfer et al., Commun. Phys. **3**, 36 (2020)